Crustal velocity variations and constraints on material properties in the Charlevoix Seismic Zone, eastern Canada

John Onwuemeka[1], Yajing Liu[1], and Rebecca M. Harrington[2]

[1]McGill University
[2]Ruhr University Bochum

November 22, 2022

Abstract

Crustal velocity variation within impact-related seismic zones is commonly attributed to mechanisms such as pore pressure changes, dense fracture network, and compositional variation. In this study, we combine seismic tomography, rock physics analysis, and potential field modeling to quantitatively investigate the mechanisms that influence crustal velocity variation in the Charlevoix Seismic Zone (CSZ), a meteorite impact-related seismic zone in eastern Canada. Earthquakes in the CSZ align along two broad NE-SW trending clusters related to reactivated paleo-rift faults. Within the impact structure, the earthquakes are diffusely distributed and lower velocity bodies are ubiquitous which can be attributed to crustal damage from tectonic inheritance exacerbated by the meteorite impact. The Bouguer gravity anomaly decreases southeastward across the St. Lawrence River due to density disparity between rocks in the Grenville Province and the Appalachians. We find a higher velocity body northeast of the impact structure that does not exhibit an observable gravity anomaly, which suggests the presence of a rock (e.g. anorthosite) of comparable density but a higher elastic moduli within another rock (e.g. charnockite). Outside the impact structure, compositional variations control velocity changes, whereas inside the impact structure, velocity variations can be explained by porosity enhancement of up to 10% by low (0.1) aspect ratio cracks. Our results suggest that intense fracturing and compositional alteration, rather than pore pressure, control velocity variations, hence earthquake processes in the CSZ.

Hosted file

`relocation.gif` available at https://authorea.com/users/538815/articles/599897-crustal-velocity-variations-and-constraints-on-material-properties-in-the-charlevoix-seismic-zone-eastern-canada

Crustal velocity variations and constraints on material properties in the Charlevoix Seismic Zone, eastern Canada

J. Onwuemeka[1*], Y. Liu[1], and R. M. Harrington[2]

[1]Department of Earth and Planetary Sciences, McGill University, Montreal, Quebec, Canada
[2]Institute of Geology, Mineralogy, and Geophysics, Ruhr University, Bochum, Germany

Key Points:

- Lower velocities and a diffuse earthquake distribution are prevalent inside the Charlevoix impact structure due to intense fracturing
- Porosity enhancement of up to 10% by low (0.1) aspect ratio cracks explain velocity variations inside the impact structure
- Compositional alteration dominates crustal seismic velocities outside the impact structure

*Current address: Dept. of Earth and Planetary Sciences, McGill University, Montreal, Quebec, Canada

Corresponding author: John Onwuemeka, `john.onwuemeka@mail.mcgill.ca`

Abstract

Crustal velocity variation within impact-related seismic zones is commonly attributed to mechanisms such as pore pressure changes, dense fracture network, and compositional variation. In this study, we combine seismic tomography, rock physics analysis, and potential field modeling to quantitatively investigate the mechanisms that influence crustal velocity variation in the Charlevoix Seismic Zone (CSZ), a meteorite impact-related seismic zone in eastern Canada. Earthquakes in the CSZ align along two broad NE-SW trending clusters related to reactivated paleo-rift faults. Within the impact structure, the earthquakes are diffusely distributed and lower velocity bodies are ubiquitous which can be attributed to crustal damage from tectonic inheritance exacerbated by the meteorite impact. The Bouguer gravity anomaly decreases southeastward across the St. Lawrence River due to density disparity between rocks in the Grenville Province and the Appalachians. We find a higher velocity body northeast of the impact structure that does not exhibit an observable gravity anomaly, which suggests the presence of a rock (e.g. anorthosite) of comparable density but a higher elastic moduli within another rock (e.g. charnockite). Outside the impact structure, compositional variations control velocity changes, whereas inside the impact structure, velocity variations can be explained by porosity enhancement of up to 10% by low (0.1) aspect ratio cracks. Our results suggest that intense fracturing and compositional alteration, rather than pore pressure, control velocity variations, hence earthquake processes in the CSZ.

1. Introduction

Intraplate seismicity occurs in stable plate interiors away from tectonic plate boundaries. The typical strain rates ($\leq 10^{-10}\ yr^{-1}$) within intraplate seismic zones are 2 or more orders of magnitude less than average strain rates ($\geq 10^{-8}\ yr^{-1}$) reported for seismogenic plate boundary faults (e.g., Gordon, 1998; Mazzotti & Adams, 2005; Mazzotti & Gueydan, 2018). Consequently, seismogenic faults in intraplate seismic zones produce moderate-to-large earthquakes (e.g., 2001 **M** 7 Bhuj earthquake, 1811-1812 ~**M** 7 New Madrid earthquakes) less frequently than their plate boundary analogues (Hough et al., 2004; Bendick et al., 2001), but their physical mechanisms remain poorly understood. Steady tectonic loading in plate interiors could be attributed to basal traction, gravitational body forces, and plate boundary forces (Liu & Stein, 2016). However, these mechanisms are not always sufficient to elevate stresses to levels that trigger failure on intraplate faults, and are unlikely to be entirely responsible for the stress budget within intraplate seismic zones. Several studies show that earthquakes within plate interiors concentrate within zones of inherited crustal weaknesses due to factors such as, tectonics, volcanism, and meterorite impacts (e.g., Bendick et al., 2001; Mazzotti & Gueydan, 2018; Sykes, 1978; Tarayoun et al., 2018). Therefore, mechanisms such as postglacial rebound, loading from distal plate boundaries, and localized lithospheric-scale structural weaknesses (i.e., stress amplifiers) due to prior tectonic episodes are collectively invoked to explain loading on seismogenic faults within intraplate seismic zones (Liu & Stein, 2016; Mazzotti & Gueydan, 2018). The structural weaknesses potentially link to dense fracture networks and density disparities. In order to better understand processes and mechanisms that control earthquake processes within intraplate seismic zones, it is important to investigate the distribution of tectonic structures such as faults, fracture zones, and material compositions due to their primary effect on crustal stresses. Such investigation is paramount to constrain physical mechanisms that control seismicity, especially for complex intraplate seismic zones such as the Charlevoix Seismic Zone (CSZ) in eastern Canada.

The CSZ is located in Quebec along the St. Lawrence paleo-rift system within the stable North American continental interior. It has been recognized as the most active seismic zone in eastern Canada (Fig. 1). Present-day geological features of the CSZ derive from previous significant tectonic episodes, including Grenville orogeny, opening of the Iapetus ocean, and Taconian orogeny, that created a weak zone which was overprinted by a late Ordovician to early Silurian meteorite impact (Rondot, 1971; Lemieux et al., 2003; Schmieder et al., 2019). The meteorite impact structure crosscuts pre-existing NE-SW trending normal faults of the St. Lawrence rift system. Major rifts within the CSZ, including Charlevoix, Gouffre River, and St. Lawrence faults, have been found to dominate distribution of seismicity in the CSZ (Onwuemeka et al., 2018; Powell & Lamontagne, 2017; Yu et al., 2016). Mesozoic reverse-sense fault reactivation due to ridge-push force following the opening of Atlantic Ocean is thought to contribute to the current stress perturbation responsible for the seismicity in the CSZ (Lemieux et al., 2003; Ma & Eaton, 2007). In addition, glacial unloading following the Wisconsin glaciation (85 - 11 kyr) is interpreted to exert post-glacial rebound stress on critically stressed faults in the pre-weakened structural zones (Wu & Hasegawa, 1996; Tarayoun et al., 2018). Historically, five **M** 6+ earthquakes occurred in the CSZ since 1663, with at least another two **M** 6+ in the past 10,000 years prior to the 1663 event based on paleo-seismic studies (Tuttle & Atkinson, 2010). The evidence of **M** 6+ events is seen in liquefaction features (e.g., basal erosion, sand dikes, and diapirs) that are typical of strong ground-shaking and fault rocks such as pseudotachylytes formed as a result of shear-related frictional melting (Lemieux et al., 2003). Previous studies (e.g., Onwuemeka et al., 2018; Yu et al., 2016) found that earthquakes in the CSZ are diffusely distributed within the impact structure, nevertheless, they broadly define two NE-SW trending clusters that highlight the high (up to 60°) dip angle of the reactivated Iapetan normal faults.

The unique, but complex, tectonic setting of the CSZ necessitates adequate assessment to quantify the contributions of the different physical mechanisms such as intense fracturing and compositional variation to its current velocity structure, and to relate the velocity structures to earthquake processes. Previous studies (e.g., Baird et al., 2010; Mazzotti, 2007; Mazzotti & Gueydan, 2018; Fadugba et al., 2019) suggest that tectonic inheritance (e.g., diffusely distributed fracture networks) acts to locally concentrate stress and potentially control the distribution of earthquakes. Variations in rock composition could similarly enhance local stresses due to lateral imbalance of gravitational potential energy caused by intramural density and shear strength disparity (Liu & Stein, 2016). Compositional variation has been suggested as a contributing factor to stress concentration in the Western Quebec seismic zone which is located southwest of the CSZ within the St. Lawrence rift system (e.g., Dineva et al., 2007). Thus, the objective of this work is to quantify the spatial extent and relative contributions of (1) intense fracturing, and (2) compositional variation on velocity variations and their control on earthquake processes in the CSZ.

Passive source seismic tomography has been used extensively to study the Earth's internal structure at different scales (e.g., Christensen & Mooney, 1995; Ebel et al., 2000; Koulakov et al., 2007, 2009b). Previous tomographic studies in the CSZ (e.g., Vlahovic et al., 2003; Powell & Lamontagne, 2017) imaged heterogeneous crustal velocities that likely represent the distribution of structural features. Vlahovic et al.

(2003) used 3093 P-wave arrival travel-times from 489 earthquakes to perform tomographic inversion and found a dearth of earthquakes near and within high-velocity bodies. Furthermore, the authors found that larger ($M_N \geq 4$) events preferably occur around the edges of high-velocity bodies, particularly at mid-crustal depth around the northeastern edge of the outer rim of the impact structure (Fig. 1). The authors imaged lower velocities at mid-crustal depths at the center of the impact structure surrounded by higher velocity bodies (Fig. 9 in Vlahovic et al., 2003). They interpret the higher velocity bodies as stronger crust surrounding less competent crust (i.e., the lower velocity bodies). Whereas crustal velocity variations can be inferred with seismic tomography, the results are non-unique therefore would be insufficient to quantify the contributions of any specific mechanism nor more accurately interpret the physical conditions of the crust. Powell and Lamontagne (2017) identified varying velocities across the entire upper to middle crust within the CSZ and suggested that both compositional variation and intense fracturing could be responsible for observed velocity variations. But, the relative contribution of these mechanisms is not yet quantitatively determined.

Rock physics analysis and potential field modeling are also powerful tools that can be used to constrain velocity variations and quantify individual contributions from the proposed physical mechanisms. The elastic modulus of a rock is influenced by its material composition as well as its mechanical properties (e.g. internal cracks). For example, an intact rock would have different elastic moduli when compared with a fractured rock of exactly the same material composition. Similarly, a compositionally altered, mechanically intact rock would have different elastic moduli relative to the unaltered state. Therefore, rock physics analysis can be used to quantify the influence of rock properties such as crack volume, crack aspect ratio, and density on the speed of seismic wave propagating through the rock, while potential field modeling (e.g., Bouguer anomaly modeling) can be used to discriminate density disparities. When combined, they can distinguish velocity changes due to compositional variation and intense fracturing. For example, contrasting velocity within an area that does not show observable Bouguer gravity anomaly disparity is mostly likely caused by conglomeration of rocks of differing elastic moduli but similar density. Roland et al. (2012) used rock physics analysis and gravity anomaly modeling to constrain seismic velocity variation at the

Quebreda-Discovery-Gofar transform faults, East Pacific Rise. In their study, they found that low-velocity zones at Gofar and Quebreda faults are explained if the porosity is enhanced by up to 8%, and ruled out material alteration such as serpentinization as a contributing mechanism.

In this study, we show the results of multi-faceted approach, including tomographic inversion, effective media analysis, and gravity modeling, to quantify the contributions of intense fracturing and rock composition to variations in crustal velocity and seismic behavior in the CSZ. We use local earthquake travel-time tomography (LET) techniques to image velocity structures. We also analyze changes to seismic wave velocity due to material properties (i.e., effective media analysis) and use gravity modeling to constrain the spatial dominance of the material property variation. The effective media analysis incorporates two crustal models, (1) fractured crust, and (2) compositionally altered crust (i.e. crust composed of heterogeneous materials), to derive 3D density models from the observed velocity model. We use the 3D density model to predict Bouguer gravity anomalies and compare the predictions to observations to constrain the mechanism(s) responsible for the velocity changes.

2. 3D velocity structure imaging

2.1. Seismograph data

Depending on the type of data, tomographic inversion can be used to image structures within a seismic zone to provide insight into structural features that control the earthquake distribution. In this study, we use P- and S-wave first arrival time picks of 2405 local earthquakes (M_N -0.6 - 5.4; M_N is Nuttli magnitude; Nuttli, 1973) reported in the Natural Resources Canada (NRCan; `https://earthquakescanada.nrcan.gc.ca/stndon/NEDB-BNDS/bulletin-en.php` last accessed August 2019) earthquake catalog (Jun. 1988 - Mar. 2019 including relocated seismicity of Onwuemeka et al., 2018) for the CSZ to invert for V_p and V_s (Fig. 1). The arrival times are recorded by fourteen CNSN stations (in operation at different times since the 1980s; 7 stations in operation since October, 1994), five Quebec-Maine Transect campaign stations (August 2012 to August 2016), three USArray Transportable Array stations (August 2003 to September 2015), and four temporary campaign stations deployed by McGill University (since July 2015; Fig. 2). The (automatically picked) phase arrival times of 1626 events reported up until May, 2012, were retrieved from Yu et al. (2016). The P- and S-wave first arrival times of the remaining 779 events are manual picks. A total of 17518 catalog travel-times (8785 for P-wave and 8733 for S-wave) were computed and used as input for the tomographic inversion. We use the St. Lawrence River south shore velocity model (Fig. S1) of (Lamontagne, 1999) as the starting 1D velocity model, as it yields lower travel-time residuals compared with the north shore model (Onwuemeka et al., 2018).

2.2. Travel-time tomography method

Travel-time tomography uses a set of known variables (e.g., phase travel-times) and *a priori* information (e.g., an initial/starting velocity model) to infer model parameters such as earthquake locations and velocity structure. The synthetic source-to-station travel-time for each source-station pair is computed based on ray theory (e.g., Zhang & Thurber, 2003). The travel-time, t_i, from source to station is given by:

$$t_i = \int_{S_i} \frac{ds}{c} \tag{1}$$

where c is the velocity model and S_i is the ith ray path. The ray path yielding the lowest residuals is accepted as the best solution.

A 3D ray coverage computed with a ray-tracing algorithm and checkerboard test provide a quantitative measure of the resolution of a given data set. To avoid bias by *a priori* information in the checkerboard resolution test, the theoretical computation of travel-time in the forward problem and inverse problem should be solved with different algorithms. Here, we use the double-difference travel-time tomography algorithm, *TomoDD*, (Zhang & Thurber, 2003) a program that computes ray paths and minimizes residuals with a pseudo-bending ray-tracing algorithm (Um & Thurber, 1987), to calculate synthetic travel-times within a checkerboard volume. For the inverse problem, we use the segmented bending ray-tracing algorithm in *LOTOS* (Koulakov, 2009a). Each individual wave ray path starts as a straight line from the source location to the observation point and it is then iteratively deflected in 3D for travel time minimization (Koulakov, 2009a). The ray path with the lowest travel-time residual is selected. *LOTOS* simultaneously inverts for source coordinates and velocity, and has the option to optimize the input 1D velocity model with the *VELEST* algorithm of Kissling et al. (1994). *LOTOS* reduces computation time relative to *TomoDD* by defining the velocity parameterization for nodes, cells, polygons, or any other parameterization. The inversion grid nodes are adaptive, and nodes without crossing-raypaths are removed to improve computation efficiency. We refer the readers to Koulakov (2009a) and references therein for more information regarding *LOTOS*.

2.3. Tomographic inversion algorithm evaluation and parameter setting

2.3.1 Checkerboard test and tomographic model setup

To test model reliability, we explore wide range of possible parameters that might affect the tomographic inversion results, including the forward solver, starting velocity model, source-station geometry, grid size, and noise. A commonly used technique for resolution analysis is the checkerboard test, which involves creating an artificial polygons of alternating velocities and simulating seismic sources within the checkered volume. To better reproduce the uncertainties in real data, we use *tomoDD* to generate the synthetic travel-times and then add 5% Gaussian noise to the travel-times to replicate noise. We generate the synthetics with alternating $\pm 10\%$ perturbations of the 1D south shore velocity model of Lamontagne (1999) within a 3D volume with checkerboard sizes of 10 km, 6 km, 5 km, and 4 km. We then invert the synthetic travel-times with *LOTOS*.

To further ensure that our synthetic travel-times have similar features common to real data and the source locations are not constrained *a priori*, we set the source epicenters to the center of our study area (latitude = 47.53, Longitude = -70.17) with depths set to 1 km, 5 km, and 10 km for different test runs. Furthermore, we use different grid node spacing (0.5, 1, and 2 km in all (x,y,z) directions) and choose the node spacing with the lowest absolute root mean square (RMS) residual as the optimum spacing for our study. Similarly, we perform a suite of inversion runs with the damping factor (D) in the range of [0, 0.3] for both P and S waves, and the smoothing factor (S) of [0.2, 0.6] for P and [0.4, 0.9] for S-waves. The optimal set of D and S are chosen as those resulting in the lowest RMS residuals, that is, [D, S] =

[0, 0.3] for P-waves and [0.3, 0.6] for S-waves. In addition, we use three different 1D starting velocity models that comprise (1) the 1D south shore, (2) a quasi layer-over-halfspace, and (3) perturbed 1D velocity models (Fig. S1). The perturbed 1D model is determined by randomized perturbation of V_p, V_s, and depth of the 1D south shore model with the random number generator function in *Python*©. We note that *LOTOS* internally accounts for the effect of grid node orientation by stacking velocities computed for 4 different grid orientations (0°, 22°, 45°, and 67° azimuths). The number of LSQR iterations for each grid orientation of the joint inversion is 200 in all resolution tests.

The inversion setup for the real data is similar to the setup for the resolution (checkerboard) tests. The optimum smoothing and damping factors are determined from the resolution analysis. Grid node spacing of 1 km in x, y, and z directions is preferred as it yields lower RMS and grid orientations are set to 0°, 22°, 45° and 67°, as in the resolution tests. We first optimize the input 1D south shore velocity model and extrapolate the optimized model to 3D as starting model for the joint inversion. The relocation steps include an initial location with the 1D starting velocity model with a grid search approach and location refinement with the segmented bending ray-tracing technique in the joint inversion step. Errors/uncertainties in the joint inversion solution are quantified by the RMS (0.068 for P-wave and 0.081 for S-wave) of the final iteration.

2.3.2 Checkerboard test results

Figures 3 & 4 show depth slices and cross-sectional views of the synthetic model and recovered features of the checkerboard test with the 10 km checkerboard, the catalog hypocenters, the south-shore 1D model as the starting velocity model, and 1 km grid spacing. The synthetic data inversion recovered most of the checkerboard features, particularly along the St. Lawrence River between the northeastern and southwestern limits where ray coverage is best (Fig. 2). The checkerboard recovery is best within the impact structure where most of the earthquakes occur. The recovered features are somewhat smeared northeast of the outer rim of the impact structure (Figs. 3 & 4) and throughout the edges of the region defined by the ray coverage (Fig. 2). The values of the recovered V_p and V_s changes are slightly higher (12-14%) than the input values (10%) in some sections of the upper 8 km, but there is high resemblance between the synthetic (checkerboard) and recovered models, particularly, down to ∼18-20 km (Fig. 4). The ∼18-20 km depth limit is consistent with the distribution of the hypocenters and ray paths (Fig. 2) as the ray density starts to diminish at greater depth.

The results of the evaluation of different parameters (starting velocity model, starting earthquake location, grid spacing, and checkerboard size) can be found in Figures S2 - S11. The high resemblance between the synthetic velocity model (checkerboard) and the recovered model is consistent across all the three different starting 1D velocity models which lends credence to the reliability of the inversion algorithm and procedure. Furthermore, the checkerboard results are not affected by the initial earthquake hypocenters, as the recovered checkerboard with the 3 sets of hypocenter distributions and the south shore 1D starting velocity model are very similar. The maximum difference in RMS between the starting hypocenter distributions is 10^{-3} for both V_p and V_s. The consistency of the recovered checkerboard with respect to the initial earthquake hypocenters is possible because the inversion algorithm first determines absolute earthquake locations before it performs joint inversion for hypocenter refinement and velocity distribution. The high- and low-velocity pattern is consistent across all the tested grid spacing (0.5, 1, 2 km). However, the 1 km grid spacing performs better than the 0.5 and 2 km spacing, as the result for the 1 km grid spacing qualitatively shows higher resemblance with the synthetic model and yields the lowest RMS values (0.056 for V_p; 0.066 for V_s). The small discrepancy between the outputs for the 0.5, 1, and 2 km grid spacing could be due to variations in ray density per grid node.

The results (Figs. 3, 4, & S4 - S6) of the different checkerboard sizes show that the recovered checkerboard model diminishes in resolution with decreasing size (i.e. the 10 km checkerboard is best resolved whereas the 4 km checkerboard is least resolved). The recovered model is ostensibly well resolved down to the 5 km checkerboard size but the features are completely obscured for the 4 km checkerboard (Figs. S5 & S6). The difference in the result is not a shortcoming of the inversion code, but may be due to changes in raypaths and ray density per node as a result of the size of the checkerboard. As in the 10 km case, the resolution of the recovered model for the 6 and 5 km cases is best along the St. Lawrence River between the northeastern and southwestern edges of the impact structure. Similarly, the vertical resolution of the 6 and 5 km checkerboards become less well resolved below ~18-20 km.

2.4. Tomographic inversion results

Figures 5 - 7 & S12 - S14 show the distribution of body wave velocities and earthquake hypocenters across the CSZ. We show five NW-SE and four NE-SW cross-sections that display V_p and V_s changes with depth (Figs. 6 & 7). Three of the NW-SE profiles run across the inner rim of the impact structure and show that velocity generally increases with depth, however with a few exceptions. Earthquake hypocenters within 1 km of each profile are projected onto the profiles. Earthquakes are diffusely distributed, especially within the impact structure, however, they follow two broader NE-SW roughly linear trends along the St. Lawrence River (Fig. 5). The two NW-SE seismicity trends sandwich a region of relatively low seismicity. Along the northern shore of St. Lawrence River, earthquakes more closely follow the outline of the major high-angle SE dipping normal faults (GRF and SLF; Figs. 1, & 5). A clearer outline of the high-angle normal faults can be seen along profiles AA' and DD' (green enclosures in Fig. 6). Within the upper 10 km, more earthquakes occur along the northern shore of St. Lawrence River than beneath the River. The distribution of seismicity across the river shows that the reactivated normal faults significantly control earthquake hypocenters in the CSZ. Although we do not observe systematic clustering of earthquakes within either lower or higher velocity bodies, visual inspection suggests that earthquakes tend to occur within lower velocity structures in some cross-sections (e.g., AA', BB' for V_s, Fig. 6). Fewer events occur inside higher velocity structures relative to the surrounding volume. A small earthquake cluster within the upper ~8 km in the Grenville basement off the northern shore (circled region in profiles EE' of Fig. 6) just above a high V_s body is indicative of rupture or slip within a segment of a northwest dipping fault. There is a similar earthquake cluster southeast of the central uplift between the topographically mapped boundaries of the inner and outer rims of the impact structure. This cluster also occur proximal to a high velocity body (circled region in profiles II' of Fig. 7). The earthquake clustering in the proximity of higher velocity structures suggest that the higher velocity structures are mechanically stronger (i.e. less likely to fail or are more able to accumulate seismic strain energy) similar to the conclusions of Michael and Eberhart-Phillips (1991) and Vlahovic et al. (2003).

A high P-wave velocity body is found northeast of the northern shore of the St. Lawrence River close to the edge of the outer rim of the impact structure (Fig. 5). This high velocity body has also been reported in previous studies (e.g., Vlahovic et al., 2003; Powell & Lamontagne, 2017). The inner rim of the impact structure is replete with low velocity bodies especially within the upper 10 km. Some of these lower velocity features roughly follow the reported surface trace of the inner rim of the impact structure. Below 10 km, the areal extent of these lower velocity bodies decrease steadily with depth. But, a low velocity body northwest of the central uplift extends down to 18 - 20 km (blue circled region in Fig. 5). However, this structure is near the northwestern limit of dense ray coverage of our data set, hence its depth and areal extent may not be well-constrained. Lower velocities also pervade the southeast portion of the impact structure, but similar to the lower velocity feature northeast of the impact structure, they are less well resolved due to the locally limited ray coverage. Generally, the lower velocity features are more pronounced for S-waves and somewhat more subtle for P-waves. The lower velocity features appear to terminate at ∼18 km (Profiles AA', BB', FF', GG' & HH' in Figs. 6 & 7). Southeastward from profile FF' towards profile II', the lower velocity features become increasingly less prominent (Fig. 7). Thus, the lower velocity features are more likely related to the damaged crust due to the meteorite impact rather than composition of crustal materials as they appear to be restricted within the topographically mapped extent of the impact structure. The resolution of structures in the 5 km checkerboard test (Fig. S5) is consistent with the interpretation that lower velocity features represent realistic seismic velocity variations, as their dimensions are larger than 5 km.

3. Rock physics analysis and gravity modeling

Following previous geophysical studies in the CSZ as well as in other seismic zones (e.g., Roland et al., 2012; Powell & Lamontagne, 2017), compositional variation and intense fracturing are suggested as probable cause(s) of velocity variations within seismic zones. There is the possibility that one or both of the aforementioned mechanisms exert significant control on velocity variations. Therefore, we also investigate the influence of mechanical and compositional variation of the basement rocks in the Charlevoix region on their body wave velocities, and model the gravity response of such alteration to establish a quantitative relation between the mechanical and compositional properties and velocity variations.

3.1. Possible mechanisms for elastic moduli and density variations

Variations in crustal velocity derive from changes in elastic moduli and density of rock materials, and are inherently non-unique. For example, consider two rocks comprised of a mixture of two mineral assemblages (phases) of comparable density, but dissimilar elastic moduli. One rock contains a higher proportion of the phase with larger elastic moduli. The second rock contains a mixture of the same phases, but with a lower proportion of the phase with larger elastic moduli, and is also permeated with fluid-filled cracks, and has a lower resulting density. The velocity responses of the two example rocks types above could be similar in spite of their differing densities and elastic moduli. One way to explore the tradeoff between varying elastic moduli and density due to material composition and crack porosity is to use the gravity response to constrain observed velocity variation.

We use the theoretical relation proposed by Hashin and Shtrikman (1963) for multi-phase media to test the hypothesis that observed velocity variations are as a result of compositional variation. Hashin and Shtrikman (1963) leveraged the variational principles (principles of minimum complimentary and minimum potential energies) in the theory of elasticity to derive a formulation for the lower and upper bounds of the effective elastic moduli of a mechanical mixture of materials with varying elastic properties. The lower and upper bounds of the bulk (K_l^*, K_u^*) and shear (μ_l^*, μ_u^*) moduli of a two-phase quasi-homogeneous medium is given by:

$$K_l^* = K_1 + \left(\frac{v_2}{\dfrac{1}{K_2 - K_1} + \dfrac{3v_1}{3K_1 + 4\mu_1}} \right) \tag{2}$$

$$K_u^* = K_2 + \left(\frac{v_1}{\dfrac{1}{K_1 - K_2} + \dfrac{3v_2}{3K_2 + 4\mu_2}} \right) \tag{3}$$

$$\mu_l^* = \mu_1 + \left(\frac{v_2}{\dfrac{1}{\mu_2 - \mu_1} + \dfrac{6v_1(K_1 + 2\mu_1)}{5\mu_1(3K_1 + 4\mu_1)}} \right) \tag{4}$$

$$\mu_u^* = \mu_2 + \left(\frac{v_1}{\dfrac{1}{\mu_1 - \mu_2} + \dfrac{6v_2(K_2 + 2\mu_2)}{5\mu_2(3K_2 + 4\mu_2)}} \right) \tag{5}$$

$$v_1 + v_2 = 1 \tag{6}$$

where K_1, K_2, μ_1, μ_2, v_1, and v_2 are the bulk and shear moduli, and volume fraction of phases 1 and 2, respectively. The separation between the lower and upper bounds of the effective (multiphase) medium is determined by the relative stiffness of the constitutive media/phases, thus provides the extremities of the bulk and shear moduli of the multiphase quasi-homogenoeus medium. The expression for a two-phase effective medium can be extended to any number of phases. Firstly, any two of the constitutive phases is treated to derive the effective medium. Then the effective medium is considered as a new, merged 'single' phase which is combined with any one of the remaining single phases to derive a new two-phase effective medium. The process is repeated until all the desired phases are added to derive an effective multiphase medium. This method enables us to mechanically mix the three most abundant basement rocks (charnockite, anorthosite, and gneiss) in the Charlevoix region (Robertson, 1968; Rivers et al., 1989) and compute the elastic moduli and density of the mixture.

The elastic moduli and densities of charnockite, anorthosite, gneiss were retrieved from Seront et al. (1993), Brown et al. (2016), Wang and Ji (2009), and Rao et al. (2008). Seront et al. (1993) found that anorthosite in Oklahoma, which is also representative of the anorthosite in the Grenville Province, contains approximately 67% anorthite. Consequently, the elastic moduli of anorthosite with at least 67% anorthite from Brown et al. (2016) is used here for effective media analysis. The elastic properties of gneisses and charnockite in Wang and Ji (2009) and Rao et al. (2008) are from type rocks in Sulu-Dabie orogenic belt, China and Tamil Nadu, India, respectively, which may differ slightly from charnockites and gneisses found in the Grenville Province. Nevertheless, each rock type analyzed by Rao et al. (2008) contains varying degrees of the major constitutive minerals, and covers a range of elastic moduli and densities. For example, the densities of the nine charnockite samples in their study range from 2.689 - 2.784 g/cm^3 and the Young's modulus ranges from 73.44 - 88.64 GPa. We therefore assume the average of the elastic properties of charnockite in Rao et al. (2008) as representative for the Grenville charnockite. The densities and composition of paragneisses analyzed in Wang and Ji (2009) fit the density and mineral composition of Grenville paragneiss analyzed in Duncan and Garland (1977) and Volkert (2019). Therefore, we also assume the elastic properties of paragneiss used in Wang and Ji (2009) here. We compute the elastic moduli of an effective medium comprising charnockite, anorthosite, and gneiss at different proportions (each of the rocks/phases is varied from 0 - 100%) and determine a 3D density model for each rock composition model from the tomographic inversion results.

Similar to the 3D velocity models, the resulting sparse density models would not contain density predictions for areas where ray coverage is poor, rendering the density model inadequate for residual gravity modeling in such areas. To address inadequacy in the derived 3D density models and avoid the under-prediction of gravity anomalies, we use a supervised machine learning approach, Multi-Layer Perceptron (MLP) neural network, to predict density distribution for the entire 3D volume of our study. The MLP algorithm can learn a non-linear function approximator from the input data and use the non-linear function through regression analysis to predict outcomes. We design our neural network architecture with the Scikit-learn machine learning python package (Pedregosa et al., 2011). Our MLP regression implementation comprises a stochastic gradient-based optimization (Kingma & Ba, 2014), 3 hidden layers of 100 neurons each (100,100,100), and a rectified linear unit function as the activation function for the hidden layers. The optimum parameters are selected based on the score of the determination coefficient, r^2, of the predictions from a set of trial values. We use feature scaling to ensure that the independent variables (latitude, longitude, and depth) of the input are on a similar scale to improve computation efficiency and prediction accuracy. The minimum cross-validation score (a measure of the skill of the prediction model, where a score of 1.0 indicates perfect data-matching prediction) for accepted predictions is set to 0.7. The cross-validation score of all the accepted models is typically 0.8 or greater. The cross-validation acceptance criterion results in 11 full 3D density models. We account for St. Lawrence River by setting the density of the water column to 1000 kg/m^3 and a uniform water depth of 200 m which is close to the deepest barthymetry (191.1 m) in our study area (`http://gdr.agg.nrcan.gc.ca/` last accessed 17 March, 2020).

We use IGMAS+©, an interactive potential field (gravity and magnetics) modeling software (Schmidt et al., 2010) to calculate the gravity anomalies, i.e., the vertical components of gravitational anomaly, of the predicted 3D density models. We retrieve a total of 2244 Bouguer anomaly measurements and 2244 topography/bathymetry data for the Charlevoix region from the geophysical data repository of NRCan (`http://gdr.agg.nrcan.gc.ca/` last accessed 17 March, 2020). The Bouguer anomaly data range from -67.29 to -12.95 mGal and the maximum distance between closest stations is 1.84 km (Fig. S15). We compare the modeled gravity anomaly to the observed Bouguer anomaly after upward continuation and quantify the similarity between the observed and modeled anomalies by a similarity measure, sm. The upward continuation of potential field data is necessary to isolate upper to mid-crustal (0-20 km; short-wavelength) features. The sm quantifies how well the predicted gravity anomaly matches observation and it is computed as a function of the correlation distance between the observed (x) and the modeled (y) gravity anomalies as follows (Székely et al., 2007):

$$sm = \frac{\overline{xy}}{\sqrt{\left(\overline{x^2} * \overline{y^2}\right)}} \tag{7}$$

Higher similarity measure indicate a closer match between the modeled and observed gravity anomalies.

A heterogeneous porosity distribution as a result of intense fracturing, possibly due to the meteorite impact, can further contribute to the spatial variation of crustal density in the Charlevoix region. Thus, we use the theoretical formulation of Kuster and Toksöz (1974) to test the intense fracturing hypothesis. Kuster and Toksöz (1974) derived the theoretical relation between elastic moduli, material density, fracture concentration, crack geometry (i.e., aspect ratio), and body wave velocity by analysing the attenuation of elastic waves in two-phase media due to a scattering effect. The alterations (i.e., cracks) are treated as inclusions embedded in a solid matrix (i.e. 'unaltered' rock mass) and the resulting two-phase media is treated as an effective medium. It is assumed that the cracks are randomly oriented and non-interacting, and the wavelength of the propagating elastic wave is much larger than the size of the cracks. The latter condition is readily met for a spheroidal inclusion. For a single spheroidal fluid-filled crack, the theoretical formulation of Kuster and Toksöz (1974) is given by:

$$K^* = (3K^* + 4\mu)\left(\frac{cT_{iijj}}{3}\right)\left(\frac{K' - K}{3K + 4\mu}\right) + K \tag{8}$$

$$\mu^* = (6\mu^*(K + 2\mu) + \mu(9K + 8\mu))\left(\frac{c(T_{ijij} - \frac{1}{3}T_{iijj})(\mu' - \mu)}{25\mu(3K + 4\mu)}\right) + \mu \tag{9}$$

$$\rho^* = \rho(1 - c) + \rho' c \tag{10}$$

where K^*,K, K', μ^*, μ, μ', ρ^*, ρ, ρ', c, and T_{iijj} & T_{ijij} are the bulk moduli of the effective medium, matrix and inclusion, shear moduli of the effective medium, matrix and inclusion, densities of the effective medium, matrix and inclusion, crack concentration (i.e. crack porosity), and functions defined by the shape of the crack, respectively (see Kuster and Toksöz (1974) for the details of T_{iijj} & T_{ijij}). For a single crack, c is equal to the crack aspect ratio, α. If the target porosity is larger than the crack aspect ratio, c is iteratively increased until the desired crack porosity is attained, i.e. crack porosity equals number of iterations multiplied by the crack aspect ratio. The above formulation allows for the determination of the influence of a wide range of crack geometries and crack porosity on seismic wave velocities. We modeled the joint effect of crack aspect ratio (10^{-3},10^{-2}, 10^{-1}), crack porosity up to 0.1 due to fluid-filled crack-like fractures, and different proportions of charnockite, anorthosite and gneiss on seismic wave velocity to derive a 3D density model for each scenario. For this test, the lower and upper bounds on elastic moduli of the composite media determined from the Hashin and Shtrikman (1963) are used to account for different proportions of charnockite, anorthosite and gneiss in the models. The same neural network framework and parameters that was for the compositional variation scenario are used to predict the density values for the entire 3D volume of the sparse 3D density models which results in 165 full 3D density models. The approach used for the compositional variation scenario of gravity anomaly modeling and comparison of modeled and observed gravity anomalies is also used for the intense fracturing scenario.

3.2. Density models and synthetic gravity anomalies

The results of effective media analysis for two-phase medium (anorthosite and water-filled cracks with the Kuster and Toksöz (1974) relation; anorthosite and gneiss with the Hashin and Shtrikman (1963) relation) are shown in (Fig. 8) to illustrate changes in elastic moduli, density, and velocity with variation in rock composition, aspect ratio, and crack porosity. For the effective medium derived with the Kuster and Toksöz (1974) theoretical formulation, the bulk modulus typically drops by 50 - 80% whereas the shear modulus decreases by up to 45% for porosities up to 0.1. The drop in bulk modulus, hence V_p, is steepest for porosities up to 0.025. The rate of reduction of bulk and shear moduli decreases with crack aspect ratio irrespective of the difference between the elastic moduli of the constitutive phases. The magnitude of elastic moduli reduction is inversely related to crack aspect ratio. This is because the amount of cracks required to achieve a given porosity increases with decreasing crack aspect ratio. For example, to achieve a porosity of 0.1, it would require 10 times more cracks of aspect ratio of 0.001 than cracks of aspect ratio of 0.01 which would result to greater reduction in elastic moduli. The rate of decrease in density does not vary with porosity and volume fraction because the density of the effective medium is controlled by the volume fraction of the constitutive phases as volume of the system remains constant.

For the effective medium derived from the Hashin and Shtrikman (1963) relation, the elastic properties of the composite medium are less affected, because the contribution of cracks and fluids to seismic wave attenuation is absent. The elastic moduli of the effective medium change nonetheless because of the difference in the elastic properties of the constitutive phases. The difference in magnitude between the upper and lower bounds of the elastic moduli and velocities of the effective medium decrease as the difference between the elastic moduli of the constitutive phases decreases (Fig. 8b).

Densities from the effective media analysis for the study area follow the pattern of the distribution of the body wave velocities (Fig. 9a, b). Generally, the densities increase with depth, however, regions of lower velocity and higher densities correspond to regions of lower and higher velocities, respectively. The neural network regression-derived 3D enhanced density model retains most of the features of the input sparse 3D density model (Fig. 9e). However, a lower density feature NW of the impact structure is shifted ~ 5 km to the northwest (e.g., Fig. S17). The shift may be a result of the feature being at the terminus of the section with dense ray coverage, resulting in fewer data points to precisely constrain the location. Features at the termini of regions of dense ray coverage are less well resolved in the neural network predictions. Interestingly, lower densities at shallow depths northwest of the study area that correspond to observed negative gravity anomalies are predicted, despite non-availability of data for that part of the input 3D model (Figs. 9a - 9d, 10a, &10e). The compositional variation model (Figs. 9b & 9d) predicts slightly higher densities than the intense fracturing model (Figs. 9a &9c). The densities of the intense fracturing model decrease southeastward from the Grenville Province towards the Appalachians, consistent with the expected dominance of lower density rocks in the Appalachians when compared to Grenville rocks at similar depths. The density distribution appears to highlight denser Grenville crustal materials underthrusting the less dense crust of the Appalachians (dashed black line in Fig. 9c). The density distribution of the compositional variation model does not show a clearly defined boundary between the Grenville and Appalachian rocks.

The observed and modeled residual gravity anomalies and their similarity measures are shown in (Fig. 10) for both the entire study area (a, e) and the section of the study area with dense ray coverage (c, g), respectively. In the similarity measure shown in Figures 10b & 10d, each vertical bar represents the percentages of anorthosite, charnockite, and gneiss in the effective medium that was used to estimate each density model for the intense fracturing scenario. The similarity values for the compositional variation scenario (Fig. 10f & 10h) represent similarity values of composite media of anorthosite and charnockite altered by addition of a third phase (gneiss) for all tested models. The similarity values increase with increasing quantity of charnockite and decreasing quantity of anorthosite in the composite media. Larger amounts of gneiss are associated with lower similarity values, suggesting that gneiss is not a prevalent rock in the study area. Conversely, larger amounts of anorthosite are associated with higher similarity values, suggesting that anorthisite is more prevalent in the study area.

The modeled gravity anomalies, especially for the intense fracturing scenario, predicted important features in the observed gravity anomalies, including positive gravity anomalies in the southwest, north, northeast, and negative gravity anomalies east-northeast of the impact structure and in the Appalachian (Fig. 10). The sm is 85% & 80% for the best intense fracturing and compositional variation models and 68% & 73% for the poorest intense fracturing and compositional variation models, respectively, for gravity anomaly predictions in areas with dense ray coverage (Figs. 10d, & 10h). The sm of the gravity anomalies predicted for the entire study area is lower, and the discrepancy between the sm of the gravity anomaly prediction for the entire study area and the area with high ray density is probably due to uncertainties in the neural network predictions. The best gravity anomaly prediction for the intense fracturing scenario was calculated with the density models comprising (1) 100% anorthosite, and (2) 20% anorthosite & 80% charnockite for the entire study area and the area with high ray density, respectively, with cracks of 0.1 aspect ratio and up to 10% fluid-filled porosity (Figs. 10a & 10c). The best gravity anomaly prediction for the compositional variation scenario was calculated with the density model of a rock volume composed of a composite media (phase 1) comprising 20% anorthosite & 80% charnockite, and 10% anorthosite & 90% charnockite altered with gneiss (phase 2) for the entire study area and the area with high ray density, respectively (Figs. 10e & 10g). The anorthosite, charnockite, and gneiss contents of the 5 best model of the intense fracturing scenario range from 10-100%, 0-90% & 0-30%, and 10-90%, 0-90% & 0-20% for the entire study area and the section with high ray density, respectively (Figs. S18 - S21).

Gravity anomalies west of the North shore of St. Lawrence River are mostly positive. whereas the gravity anomalies east of the northern shore are negative for both the observed and modeled data. This is because of the mass deficiency over St. Lawrence River and the lower density Appalachian rocks. The negative gravity anomalies northwest of the impact structure is an exception to this general observation and could be due to the presence of a less dense rock isolated among denser rocks. There are no structural feature that show large scale mass deficiency that might be responsible for the negative gravity anomaly (Fig. S16). Alternatively, the negative gravity anomaly could be an artifact of data sparsity, as there are few observations within the area (Fig. S15a).

4. Discussion

4.1. Importance of robust tomographic resolution test

The multi-faceted approach to the travel-time tomography problem in this paper addresses several sources of bias, including forward solver, source-station geometries, starting velocity model, and noise. For example, the checkerboard test enables disregarding potential sources of error in the synthetic travel-time predictions, because the forward solver and model parameterization in the synthetic data set travel-time prediction algorithm (*TomoDD*) are different from those used for the inversion (*LOTOS*). Furthermore, using different source-receiver geometries in the synthetic travel-time computation and their reconstruction helps ensure the robustness of the tomographic inversion procedure and improve reliability of the results. For example, the earthquake hypocenters are set to arbitrary locations within the 3D volume prescribed in the checkerboard reconstruction with noise added to the synthetic travel times. We also test different model grid sizes and 1D starting velocity models, including a randomized 1D model, where the recovered checkerboard models are consistent in all cases (Figs. 3, 4, & S2 - S11). The travel-time tomography setup and approach are designed to identify and resolve biases from possible errors in forward solvers, and inversion routines that are often masked and unidentified with too much *a priori* information. This approach subjects the synthetic travel times to the conditions of real data as much as possible.

Subjecting synthetic data to the conditions of a real data does not aim to further impose nonuniqueness in the solution, because seismic tomography solutions are inherently nonunique, even for overdetermined problems (Rawlinson et al., 2014). Rather, the objective is to evaluate the aptness of the algorithm to resolve features buried in noisy data (i.e., data with some imprecise arrival time picks and/or erroneous origin times). Figures S5 & S6 show that structural features on the scale of 5 km or larger can be resolved, such as the lower velocities observed within the impact structure (Figs. 5 - 7) that likely highlight highly fractured crustal rocks.

4.2. Zones of weakness in the CSZ

The distribution of earthquake hypocenters in the CSZ highlights complex fault structures developed from the tectonic history and the overprinting of the meteorite impact. Previous studies (e.g., Yu et al., 2016; Onwuemeka et al., 2018) noted that earthquakes are more diffusely distributed within the impact structure due to a highly fractured volume, especially within the upper 20 km. The earthquake epicenters broadly show two northeast-southwest alignments with more scatter within the impact structure (Fig. 5 - 7 & S12). The depth of the earthquakes increases towards the northeast outside of the impact structure and towards the southeast. As the impact structure is hypothesized to form a bowl-shaped structure that decreases in depth away from the center, the deeper events possibly highlight the extent of active faulting processes on the planes of the Iapetus rift faults. A region of lower seismicity between the two broad northeast-southwest seismicity belts (Fig. 5) may indicate accumulated strain energy is released in aseismic deformation modes, or strain accumulation that may be released in a large event.

Despite a diffuse distribution within the impact structure, earthquakes around the northern shoreline highlight southeastward dipping faults (green circled region in Figure 6). The distribution of earthquakes across profiles AA' and BB' in Figure 6 describes what could be an outline of the more damaged segment of the impact region. Further northwest, the hypocenters project onto what is possibly the Gouffre River Fault plane. The southest dipping hypocenter distribution is particularly clear on profiles that are further away from the center of the impact structure. The trend of the hypocenters shown in Fig. 6 indicates that at least the Grouffre River Fault, and possibly the St. Lawrence and Charlevoix faults (Fig. 1), are high-angle normal faults dipping at $\sim 60°$ SE that likely developed during the breakup of supercontinent Rodinia (Kumarapeli & Saull, 1966) and was reactivated in a reverse sense under the current stress regime. The geodynamic model of Fadugba et al. (2019) indicates that the St. Lawrence rift fault dips by up to 70° within the vicinity of the CSZ. Yu et al. (2016) made a similar interpretation of high-angle dipping normal faults, namely, the Gouffre River, St. Lawrence, and Charlevoix faults, based on the distribution of relocated seismicity. Thus, the relocated seismicity distribution from our joint inversion is consistent with the results from independent methods, and likely elucidates the geometry of the major seismogenic faults in the CSZ.

4.3. Constraints on velocity variations

Several regions of high and low velocities are elucidated within the CSZ and are clearly associated with earthquake hypocenters (Fig. 6). The velocity variation is consistent with the complexity of the crust due to the many tectonic events that significantly altered the rocks and created distributed faults and fracture systems. Higher velocities are observed northeast of the inner rim of the impact structure at mid-crustal depth and lower velocities are ubiquitous within it due to a shattered crust. The higher velocity region does not correlate with higher Bouguer anomaly, and is probably due to rock bodies of comparable density with surrounding rock masses but of higher elastic moduli. For example, the density of anorthosite (2720 kg/m^3) is comparable to the density of charnockite (2735 kg/m^3); a density contrast of 15 kg/m^3 would produce a negligible gravity anomaly. For instance, the spherical equivalent of a structure with dimension of about 20 km length, 15 km width, and 8 km thick, and assuming density contrast of 15 kg/m^3 would produce a gravity anomaly of 1.8 mGal. However, the elastic moduli of anorthosite and charnockite are sufficiently different to yield a velocity contrast of at least 12%. Therefore, the velocity variation northeast of the impact structure is most likely due to compositional variation with the effective medium composed of anorthosite and charnockite or rocks of similar contrast in mechanical and elastic properties. Earthquakes of larger magnitudes occur within or around this higher velocity region (e.g., Vlahovic et al., 2003), which suggests it is comprised of rocks that are mechanically stronger hence, able to accumulate more strain energy than the surrounding material. Michael and Eberhart-Phillips (1991) studied relations between material properties of rocks and fault behaviour on the San Andreas fault system. The authors constrained the 3D V_p model and found that regions of high V_p correlate with high moment release and have a higher propensity to accumulate strain energy which is subsequently released in larger events. Our interpretation of the mechanical strength of the high velocity body are consistent with the studies cited above.

The lower V_p and V_s values observed within the inner rim of the impact structure are seismic manifestation of damaged CSZ crust due to either prevalence of high crack density/porosity, low aspect ratio cracks, varying quartz and feldspar concentration, or a combination of the above factors (Christensen & Mooney, 1995; Christensen, 1996). For example, low aspect ratio cracks disproportionately lower P-wave velocities in comparison to S-wave velocities due to larger decreases in the bulk modulus relative to the shear modulus (e.g., Shearer, 1988), and typically result in lower V_p/V_s ratios. High crack density reduces both V_p and V_s, and depending on the volume of the void space in the cracks and anisotropy, V_s may be disproportionately lower than V_p. Rocks rich in plagioclase feldspar exhibit higher Poisson's ratios, hence higher V_p/V_s than granitic rocks due to high anorthite and quartz contents, respectively (Christensen, 1996). The lower V_s and high V_p/V_s observed within the impact structure (Figs. 5 - 7, S13 & S14) would suggest high crack density, low quartz and high anorthite content, and high aspect ratio cracks. However, among all the density models tested, the effective medium comprising cracks of aspect ratio corresponding to 0.1, low quartz and high anorthite concentration produce residual gravity anomalies that best fit the observations (Figs. 9 & 10), which indicate that though the aspect ratio is low, high crack density and high anorthite concentration are dominant causative mechanisms for the observed high V_p/V_s values. The low quartz content interpretation is in agreement with what Figures 10c & 10d clearly show that similarity measure increases with decreasing gneiss content.

Several studies have suggested that observed velocity variations in the CSZ, especially within the impact structure, could be due to high pore-pressure, high crack density, and/or compositional variation. For example, Powell and Lamontagne (2017) postulate that compositional variation models best explain several observed velocity variations in the CSZ. Powell and Lamontagne (2017) further suggests that increased pore pressure in cracks with high aspect ratios explains observed seismicity and low V_p/V_s especially within the upper 8 km along the eastern rim of the impact structure. Similar to Powell and Lamontagne (2017), we find that V_p/V_s values in the upper 9-10 km within the impact structure are 1.7 or lower but higher below the upper 9-10 km which could be due to the generally observed phenomenon of increasing V_p/V_s with depth as silica content decreases (e.g., Christensen & Mooney, 1995; Christensen, 1996). The unusually high V_p/V_s ratio below 10 km could be due to disproportionately higher V_p relative to V_s within the impact structure, which supports our proposition that a combination of low crack aspect ratio and high crack density due to the meteorite impact, and increasing anorthite content better explain observed velocity variations. Although, in general, seismic velocities decrease with increasing crack density (e.g., Hadley, 1976), decreasing quartz and increasing anorthite content could dominate and produce higher V_p/V_s values. Furthermore, in subduction zones, it has been observed that high V_p/V_s is associated with overpressured rock with the increased fluid content originating from dehydration of hydrous minerals from subducting oceanic crust and mantle at shallow depth and serpentinization deeper in the subduction zone (e.g., Peacock, 1990; Audet et al., 2009). However such mechanisms and conditions for transport of water to depth greater than $\sim$ 10 km is non-existent in the CSZ, and there is currently no active regional metamorphism in Grenville Province. Consequently, precipitation of fluid due to metamorphic alterations is not ongoing. Also, the range of stress drop values (2-200 MPa; majority of the stress drop values are between 10 and 100 MPa) reported for the CSZ indicates that high pore pressure is unlikely present during CSZ earthquake ruptures (Onwuemeka et al., 2018). Therefore, assumptions of high pore-pressure as the main mechanism of fault strength reduction does not adequately explain earthquake processes and velocity variation in the CSZ.

Mazzotti and Townend (2010) considered two scenarios that could explain observed maximum horizontal (S_H) stress re-orientation in the St. Lawrence rift system: (1) high coefficient of friction and low pore pressure, which implies differential stress perturbations of 160-250 MPa, and (2) low coefficient of friction or high pore pressure which implies stress perturbations of up to $\sim$ 20-40 MPa at mid-seismogenic depths. Given that post-glacial isostatic rebound stress is probably a major source of stress perturbation in the CSZ (Wu & Hasegawa, 1996; Tarayoun et al., 2018), albeit low in magnitude ($\sim$ 10 MPa), post-glacial rebound stresses would require stress amplification to raise fault loading stress high enough to overcome fault strength. Onwuemeka et al. (2018) found that stress drop values within the impact structure could be more than one order of magnitude higher than stress drop values of earthquakes located outside of it, which implies that faults within the structure, most of which are related to the meteorite impact, are less mature with relatively stronger asperities than the paleorift faults prevalent outside the structure. Stronger asperity, typical of immature faults, is a fault strength enhancement ingredient (e.g., Viegas et al., 2010). Stronger faults would require higher stress levels, especially in the absence of elevated pore pressure, to overcome frictional strength and initiate slip which could result in higher stress drops. The stress drop discrepancy clearly shows that seismogenic faults within the impact structure exhibit a high coefficient of friction consistent with the low pore pressure and high coefficient of friction model invoked by Mazzotti and Townend (2010) as a possible explanation for S_H re-orientaion in the CSZ. Given that intense fracturing due to tectonic inheritance can amplify crustal stresses by up to a factor of 10 (e.g., Mazzotti & Townend, 2010), stress perturbation under the condition of high frictional coefficient and low pore-pressure is sufficient to explain observed maximum horizontal stress re-orientation in the CSZ, thus offering another piece of evidence that suggests crustal weakening due to intense fracturing explains velocity variations and the seismicity distribution within the impact structure (Figs. 9 & 10). Outside the impact structure, observed velocity variations are more related to compositional variation rather than intense fracturing. Therefore, our effective media analysis points to different dominant mechanisms for the spatial variations of seismic velocity in the CSZ.

5. Conclusion

To achieve robust assessment of tomography inversion algorithms and reliable results, we propose a checkerboard test methodology where synthetic travel-times are predicted with a forward solver that is different from the forward solver in the inversion framework. Furthermore, synthetic travel-times must be subjected to the conditions of real data, for example, by adding noise, using different source-station geometry, and using a starting velocity model that is different from the checkered synthetic velocity model. Such an approach yields a more unbiased report of the robustness of the tomographic inversion framework.

Applying the methodology to a joint tomography inversion for the Charlevoix Seismic Zone in eastern Canada, we find that relocated hypocenters broadly define two NE-SW seismicity clusters separated by a region of lower seismicity, which is probably due a general lack of seismically active faults or faults that exhibit aseismic deformation modes. The hypocenters image what is likely SE-dipping Iapetan normal faults, namely Gouffre River, St. Lawrence and Charlevoix faults, among other possible fault structures, and the normal faults are disrupted within the impact structure. The westernmost imaged fault structure (Gouffre River Fault) dips $\sim 60°$ SE, consistent with the dip angles reported in previous studies. More distributed seismicity within the impact structure is related to highly damaged crust due to a late Ordovician to early Silurian meteorite impact. Lower velocity structures are ubiquitous within the impact structure, which is consistent with seismic velocity reduction due to a heavily damaged crust. A higher velocity region northeast of the impact structure boundary represent a more competent crust and is associated with larger magnitude events due to its greater propensity for strain energy accumulation. This higher velocity region is indicative of a comglomeration of at least two rocks (e.g., anorthosite and charnockite) of similar density but disparate elastic moduli, as there is no discernible gravity anomaly with the surrounding rocks.

Effective media analysis and gravity modeling reduced non-uniqueness in the tomography results and helped constrain the physical mechanisms (i.e., compositional variation and intense fracturing) that dominate velocity variations in the CSZ. Velocity variations within the impact structure can be explained by highly fractured crust replete with cracks of ~ 0.1 aspect ratio with porosity enhancement of up to 10%. Outside the impact structure, compositional variations control seismic velocities. Therefore, intense fracturing and compositional variation strongly influence velocity variations and thereby seismogenesis in the CSZ, rendering elevated pore fluid pressure a less likely dominant mechanism.

Acknowledgments

The authors are grateful to Dr. Sabine Schmidt and Dr. Hans-Jürgen Götze for providing a free copy of their potential field modeling software, *IGMAS+*©. We thank Dr. Ivan Koulakov for sharing the latest version of his 3D tomographic inversion code, *LOTOS*. Older versions of *LOTOS* are available at `http://www.ivan-art.com/science/LOTOS/`. All numerical computations were performed with open-source software, *Python*©. We thank Pierre Arch his assistance in the maintenance of the McGill stations in Charlevoix. We acknowledge earthquake catalog, Bouguer anomaly and bathymetry data from NRCan (`https://www.earthquakescanada.nrcan.gc.ca/stndon/AutoDRM/autodrm_req-en.php` and `http://gdr.agg.nrcan.gc.ca/`), and waveform data from Incorporated Research Institutions for Seismology (`http://ds.iris.edu/gmap/#network=X8,CN&planet=earth`). Relocated hypocenters and the 3D velocity model presented in this paper can be accessed at `http://www.eps.mcgill.ca/~jonwueme/out/CSZ02/`. This work is supported by the Team Research Program of the Fonds de Recherche du Québec–Nature et Technologies (PR-191259).

References

Audet, P., Bostock, M. G., Christensen, N. I., & Peacock, S. M. (2009). Seismic evidence for overpressured subducted oceanic crust and megathrust fault sealing. *Nature*, *457*(7225), 76–78.

Baird, A., McKinnon, S., & Godin, L. (2010). Relationship between structures, stress and seismicity in the charlevoix seismic zone revealed by 3-d geomechanical models: Implications for the seismotectonics of continental interiors. *Journal of Geophysical Research: Solid Earth*, *115*(B11).

Bendick, R., Bilham, R., Fielding, E., Gaur, V., Hough, S., Kier, G., … Mukul, M. (2001). The 26 january 2001 “republic day” earthquake, india. *Seismological Research Letters*, *72*(3), 328–335.

Brown, J. M., Angel, R. J., & Ross, N. L. (2016). Elasticity of plagioclase feldspars. *Journal of Geophysical Research: Solid Earth*, *121*(2), 663–675.

Christensen, N. I. (1996). Poisson’s ratio and crustal seismology. *Journal of Geophysical Research: Solid Earth*, *101*(B2), 3139–3156.

Christensen, N. I., & Mooney, W. D. (1995). Seismic velocity structure and composition of the continental crust: A global view. *Journal of Geophysical Research: Solid Earth*, *100*(B6), 9761–9788.

Dineva, S., Eaton, D., Ma, S., & Mereu, R. (2007). The october 2005 georgian bay, canada, earthquake sequence: Mafic dykes and their role in the mechanical heterogeneity of precambrian crust. *Bulletin of the Seismological Society of America*, *97*(2), 457–473.

Duncan, P., & Garland, G. (1977). A gravity study of the saguenay area, quebec. *Canadian Journal of Earth Sciences*, *14*(2), 145–152.

Ebel, J. E., Bonjer, K.-P., & Oncescu, M. C. (2000). Paleoseismicity: Seismicity evidence for past large earthquakes. *Seismological Research Letters*, *71*(2), 283–294.

Fadugba, O. I., Choi, E., & Powell, C. A. (2019). Effects of preexisting structures on the seismicity of the charlevoix seismic zone. *Journal of Geophysical Research: Solid Earth*, *124*(7), 7370–7386.

Gordon, R. G. (1998). The plate tectonic approximation: Plate nonrigidity, diffuse plate boundaries, and global plate reconstructions. *Annual Review of Earth and Planetary Sciences*, *26*(1), 615–642.

Hadley, K. (1976). Comparison of calculated and observed crack densities and seismic velocities in westerly granite. *Journal of Geophysical Research*, *81*(20), 3484–3494.

Hashin, Z., & Shtrikman, S. (1963). A variational approach to the theory of the elastic behaviour of multiphase materials. *Journal of the Mechanics and Physics of Solids*, *11*(2), 127–140.

Hough, S. E., et al. (2004). Scientific overview and historical context of the 1811-1812 new madrid earthquake sequence. *Annals of Geophysics*.

Kingma, D. P., & Ba, J. (2014). Adam: A method for stochastic optimization. *arXiv preprint arXiv:1412.6980*.

Kissling, E., Ellsworth, W., Eberhart-Phillips, D., & Kradolfer, U. (1994). Initial reference models in local earthquake tomography. *Journal of Geophysical Research: Solid Earth*, *99*(B10), 19635–19646.

Koulakov, I. (2009a). Lotos code for local earthquake tomographic inversion: Benchmarks for testing tomographic algorithms. *Bulletin of the Seismological*

Society of America, *99*(1), 194–214.

Koulakov, I., Bohm, M., Asch, G., Lühr, B.-G., Manzanares, A., Brotopuspito, K., ... others (2007). P and s velocity structure of the crust and the upper mantle beneath central java from local tomography inversion. *Journal of Geophysical Research: Solid Earth*, *112*(B8).

Koulakov, I., Kaban, M., Tesauro, M., & Cloetingh, S. (2009b). P-and s-velocity anomalies in the upper mantle beneath europe from tomographic inversion of isc data. *Geophysical Journal International*, *179*(1), 345–366.

Kumarapeli, P., & Saull, V. A. (1966). The st. lawrence valley system: a north american equivalent of the east african rift valley system. *Canadian Journal of Earth Sciences*, *3*(5), 639–658.

Kuster, G. T., & Toksöz, M. N. (1974). Velocity and attenuation of seismic waves in two-phase media: Part i. theoretical formulations. *Geophysics*, *39*(5), 587–606.

Lamontagne, M. (1999). Rheological and geological constraints on the earthquake distribution in the charlevoix seismic zone, quebec, canada. *Ph.D. thesis, Carleton University, (Geological Survey of Canada Open File Report D-3778).*

Lemieux, Y., Tremblay, A., & Lavoie, D. (2003). Structural analysis of supracrustal faults in the charlevoix area, quebec: relation to impact cratering and the st-laurent fault system. *Canadian Journal of Earth Sciences*, *40*(2), 221–235.

Liu, M., & Stein, S. (2016). Mid-continental earthquakes: Spatiotemporal occurrences, causes, and hazards. *Earth-Science Reviews*, *162*, 364–386.

Ma, S., & Eaton, D. W. (2007). Western quebec seismic zone (canada): Clustered, midcrustal seismicity along a mesozoic hot spot track. *Journal of Geophysical Research: Solid Earth*, *112*(B6).

Mazzotti, S. (2007). Geodynamic models for earthquake studies in intraplate north america. *SPECIAL PAPERS-GEOLOGICAL SOCIETY OF AMERICA*, *425*, 17.

Mazzotti, S., & Adams, J. (2005). Rates and uncertainties on seismic moment and deformation in eastern canada. *Journal of Geophysical Research: Solid Earth*, *110*(B9).

Mazzotti, S., & Gueydan, F. (2018). Control of tectonic inheritance on continental intraplate strain rate and seismicity. *Tectonophysics*, *746*, 602–610.

Mazzotti, S., & Townend, J. (2010). State of stress in central and eastern north american seismic zones. *Lithosphere*, *2*(2), 76–83.

Michael, A. J., & Eberhart-Phillips, D. (1991). Relations among fault behavior, subsurface geology, and three-dimensional velocity models. *Science*, *253*(5020), 651–654.

Nuttli, O. W. (1973). Seismic wave attenuation and magnitude relations for eastern north america. *Journal of Geophysical Research*, *78*(5), 876–885.

Onwuemeka, J., Liu, Y., & Harrington, R. M. (2018). Earthquake stress drop in the charlevoix seismic zone, eastern canada. *Geophysical Research Letters*, *45*(22), 12–226.

Peacock, S. A. (1990). Fluid processes in subduction zones. *Science*, *248*(4953), 329–337.

Pedregosa, F., Varoquaux, G., Gramfort, A., Michel, V., Thirion, B., Grisel, O., ... Duchesnay, E. (2011). Scikit-learn: Machine learning in Python. *Journal of Machine Learning Research*, *12*, 2825–2830.

Powell, C. A., & Lamontagne, M. (2017). Velocity models and hypocenter relocations for the charlevoix seismic zone. *Journal of Geophysical Research: Solid Earth*, *122*(8), 6685–6702.

Rao, M., Lakshmi, K. P., Chary, K., & Vijayakumar, N. (2008). Elastic properties of charnockites and associated granitoid gneisses of kudankulam, tamil nadu, india. *Current Science*, 1285–1291.

Rawlinson, N., Fichtner, A., Sambridge, M., & Young, M. K. (2014). Seismic tomography and the assessment of uncertainty. In *Advances in geophysics* (Vol. 55, pp. 1–76). Elsevier.

Rivers, T., Martignole, J., Gower, C., & Davidson, A. (1989). New tectonic divisions of the grenville province, southeast canadian shield. *Tectonics*, *8*(1), 63–84.

Robertson, P. (1968). La malbaie structure, quebec—a palaeozoic meteorite impact site. *Meteoritics*, *4*(2), 89–112.

Roland, E., Lizarralde, D., McGuire, J. J., & Collins, J. A. (2012). Seismic velocity constraints on the material properties that control earthquake behavior at the quebrada-discovery-gofar transform faults, east pacific rise. *Journal of Geophysical Research: Solid Earth*, *117*(B11).

Rondot, J. (1971). Impactite of the charlevoix structure, quebec, canada. *Journal of Geophysical Research*, *76*(23), 5414–5423.

Schmidt, S., Götze, H.-J., Fichler, C., & Alvers, M. (2010). Igmas+–a new 3d gravity, ftg and magnetic modeling software. *GEO-INFORMATIK Die Welt im Netz, edited by: Zipf, A., Behncke, K., Hillen, F., and Scheffermeyer, J., Akademische Verlagsgesellschaft AKA GmbH, Heidelberg, Germany*, 57–63.

Schmieder, M., Shaulis, B. J., Lapen, T. J., Buchner, E., & Kring, D. A. (2019). In situ u–pb analysis of shocked zircon from the charlevoix impact structure, québec, canada. *Meteoritics & Planetary Science*.

Seront, B., Mainprice, D., & Christensen, N. I. (1993). A determination of the three-dimensional seismic properties of anorthosite: Comparison between values calculated from the petrofabric and direct laboratory measurements. *Journal of Geophysical Research: Solid Earth*, *98*(B2), 2209–2221.

Shearer, P. M. (1988). Cracked media, poisson's ratio and the structure of the upper oceanic crust. *Geophysical Journal International*, *92*(2), 357–362.

Sykes, L. R. (1978). Intraplate seismicity, reactivation of preexisting zones of weakness, alkaline magmatism, and other tectonism postdating continental fragmentation. *Reviews of Geophysics*, *16*(4), 621–688.

Székely, G. J., Rizzo, M. L., Bakirov, N. K., et al. (2007). Measuring and testing dependence by correlation of distances. *The annals of statistics*, *35*(6), 2769–2794.

Tarayoun, A., Mazzotti, S., Craymer, M., & Henton, J. (2018). Structural inheritance control on intraplate present-day deformation: Gps strain rate variations in the saint lawrence valley, eastern canada. *Journal of Geophysical Research: Solid Earth*, *123*(8), 7004–7020.

Tuttle, M. P., & Atkinson, G. M. (2010). Localization of large earthquakes in the charlevoix seismic zone, quebec, canada, during the past 10,000 years. *Seismological Research Letters*, *81*(1), 140–147.

Um, J., & Thurber, C. (1987). A fast algorithm for two-point seismic ray tracing. *Bulletin of the Seismological Society of America*, *77*(3), 972–986.

Viegas, G., Abercrombie, R. E., & Kim, W.-Y. (2010). The 2002 m5 au sable forks, ny, earthquake sequence: Source scaling relationships and energy budget. *Journal of Geophysical Research: Solid Earth*, *115*(B7).

Vlahovic, G., Powell, C., & Lamontagne, M. (2003). A three-dimensional p wave velocity model for the charlevoix seismic zone, quebec, canada. *Journal of*

Geophysical Research: Solid Earth, *108*(B9).

Volkert, R. A. (2019). Constraints from geochemistry and field relationships for the origin of kornerupine-bearing gneiss from the grenvillian new jersey highlands and implications for the source of boron. *Minerals*, *9*(7), 431.

Wang, Q., & Ji, S. (2009). Poisson's ratios of crystalline rocks as a function of hydrostatic confining pressure. *Journal of Geophysical Research: Solid Earth*, *114*(B9).

Wu, P., & Hasegawa, H. S. (1996). Induced stresses and fault potential in eastern canada due to a realistic load: a preliminary analysis. *Geophysical Journal International*, *127*(1), 215–229.

Yu, H., Liu, Y., Harrington, R. M., & Lamontagne, M. (2016). Seismicity along st. lawrence paleorift faults overprinted by a meteorite impact structure in charlevoix, québec, eastern canada. *Bulletin of the Seismological Society of America*, *106*(6), 2663–2673.

Zhang, H., & Thurber, C. H. (2003). Double-difference tomography: The method and its application to the hayward fault, california. *Bulletin of the Seismological Society of America*, *93*(5), 1875–1889.

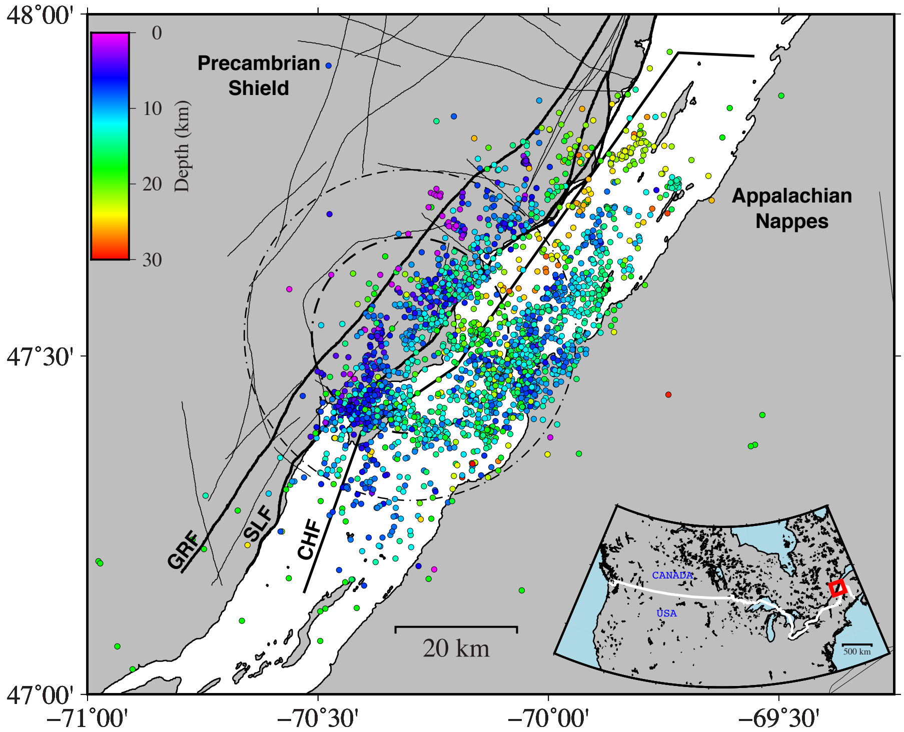

Figure 1. Distribution of 2405 earthquakes reported by Natural Resources Canada (NRCan) between January 1988 and March 2019 color-coded by depth. Dashed circles represent the inner and outer rims of the Charlevoix meteorite impact structure originally mapped by Rondot (1971). CHF, GRF, and SLF correspond to Charlevoix, Gouffre River, and St. Lawrence faults, some of the major normal faults of the St. Lawrence rift system (e.g., Yu et al., 2016). Bottom-right inset: Red box represents the location of the study area within the North American continent.

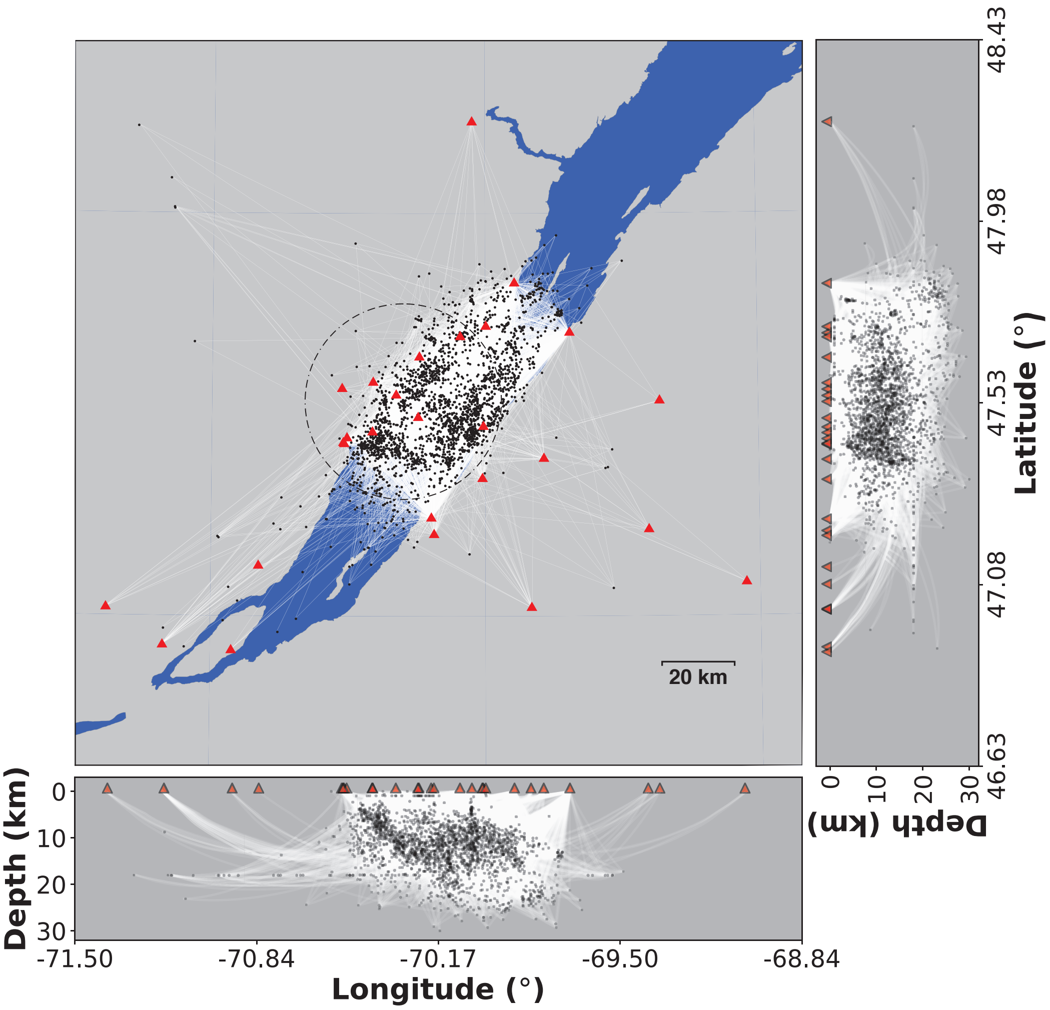

Figure 2. Ray density of the study area. White lines, black dots, and red triangles represent ray paths, earthquakes, and seismic stations respectively. Blue area denotes the St. Lawrence River. Depth cross-sectional views of ray density are shown to the right and at the bottom.

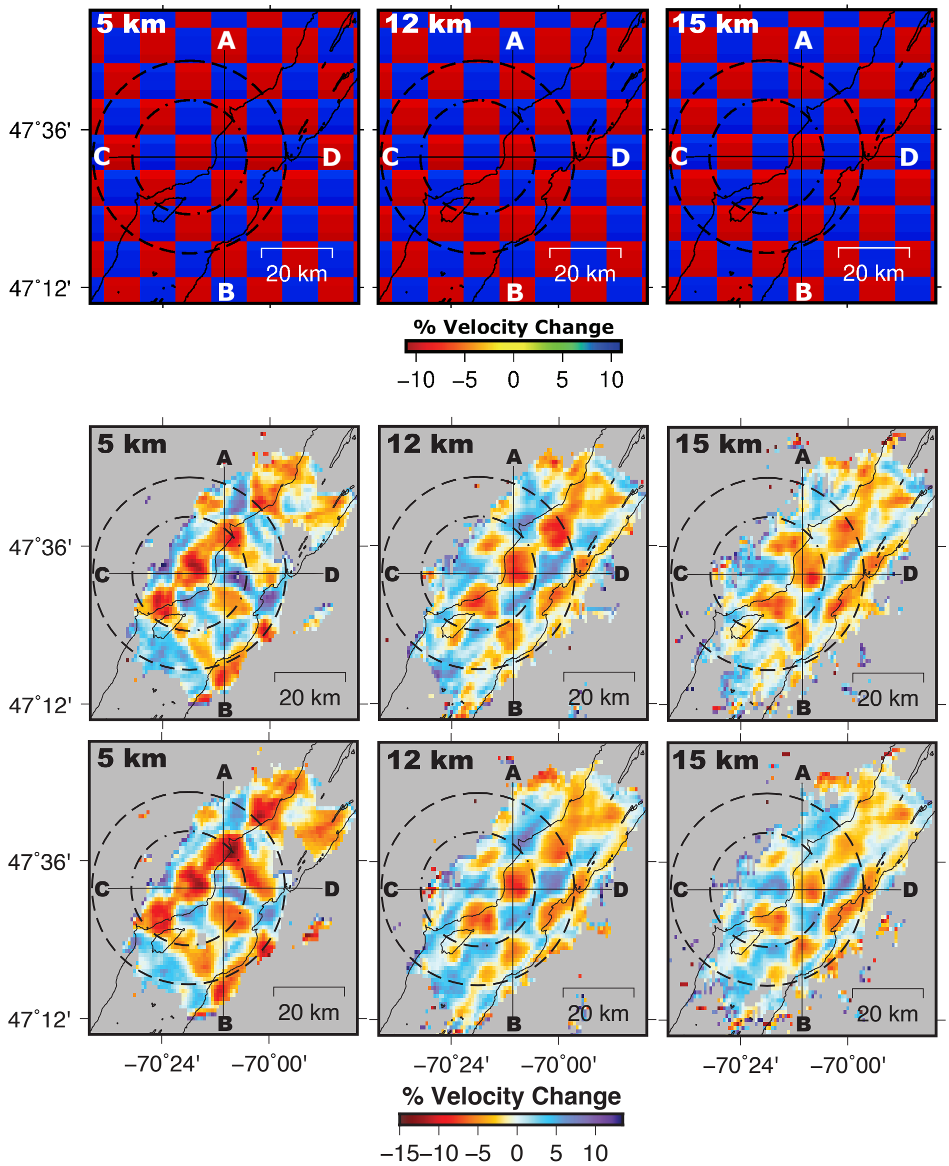

Figure 3. Checkerboard resolution test results for 10 km (left panel), 12 km (middle panel), and 15 km (right panel) depth slices. The top panel shows depth slices of the input model and the blocks (10 × 10 km each) represent ±10% alternating perturbations of the south shore 1D velocity model of Lamontagne (1999). The middle and bottom panels are the recovered checkerboard for P-waves and S-waves variations respectively. Vertical cross-sections along Profiles AB and CD are shown in Fig. 4.

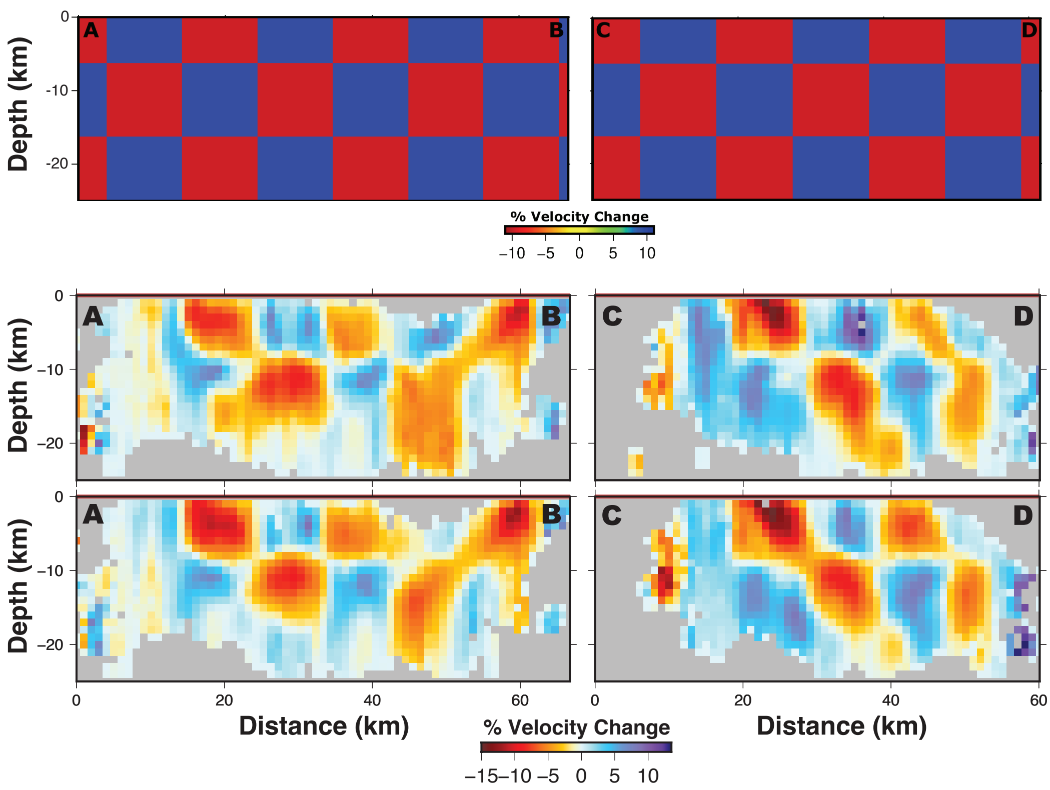

Figure 4. Vertical cross-sections of the checkerboard resolution test results as shown in Fig. 3. The top panel shows the input model of alternating blocks with ±10% velocity perturbations. The middle and bottom panels are the recovered checkerboard for P-waves and S-waves variations respectively. Profiles AB and CD are indicated in Fig. 3.

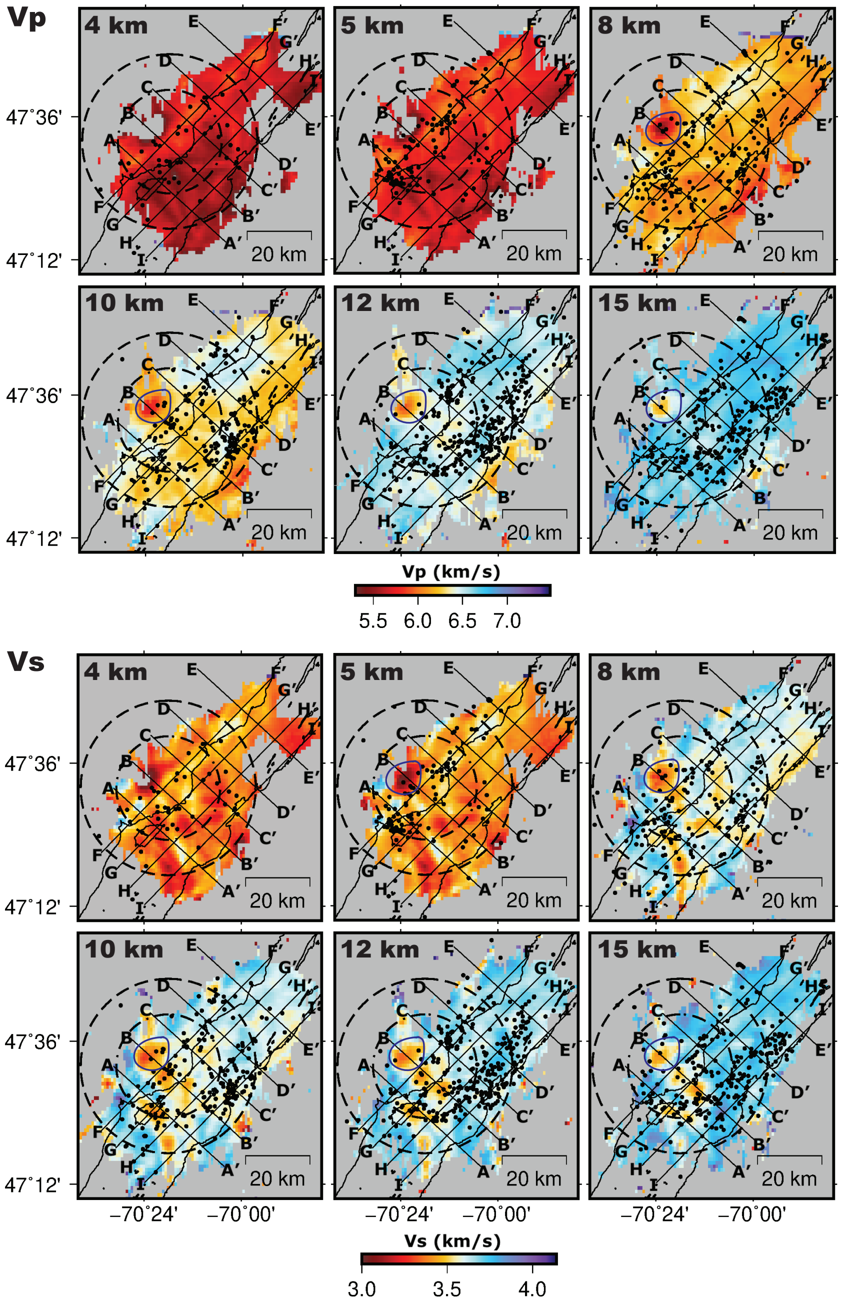

Figure 5. Depth slices of the absolute P- and S-wave velocities across the CSZ. The depth of each slice is indicated in each sub-figure. Black circles represent earthquakes located within 1 km of each depth slice. Black lines AA′-II′ represent locations of profile lines in Fig. 4. Scale bars show range of V_p and V_s. Blue circled region highlights a lower velocity feature NW of the central uplift of the impact structure.

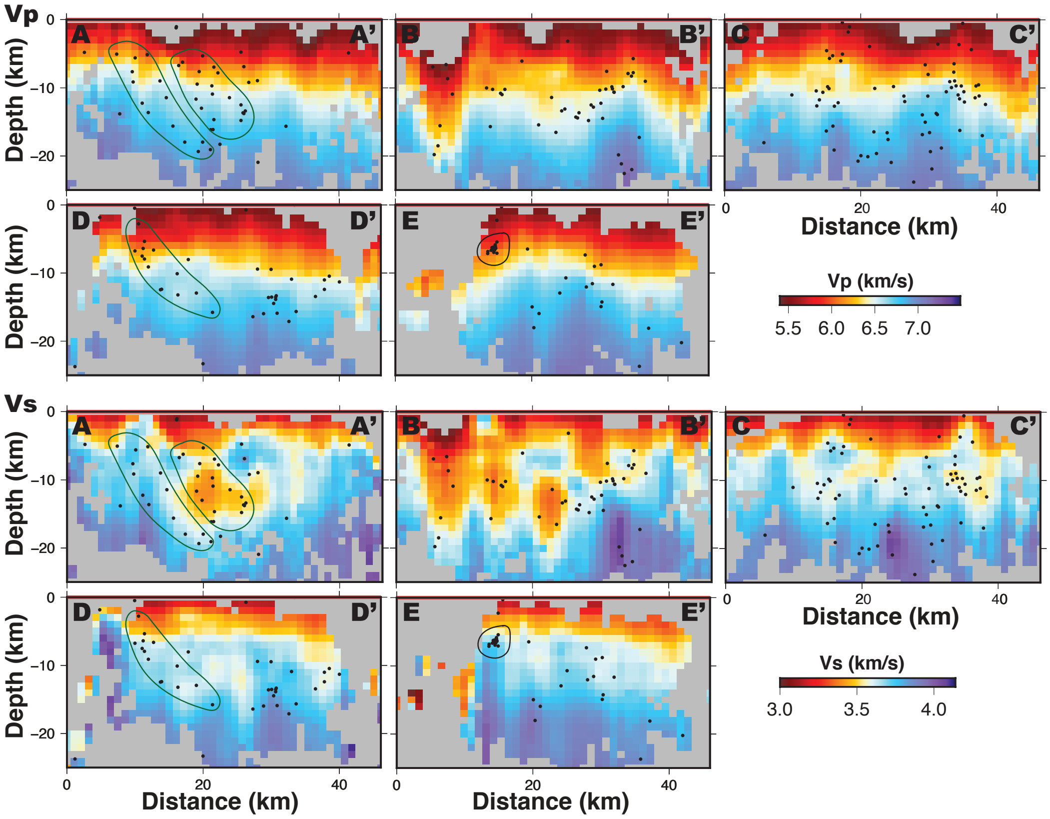

Figure 6. Vertical cross sections of profiles AA′-EE′ for V_p (rows 1 & 2), and V_s (rows 3 & 4). Profile lines are shown in Fig. 5. Black circle highlights an earthquake cluster in the upper crust NE of the impact structure. Green ovals highlight seismicity along the Iapetan normal faults.

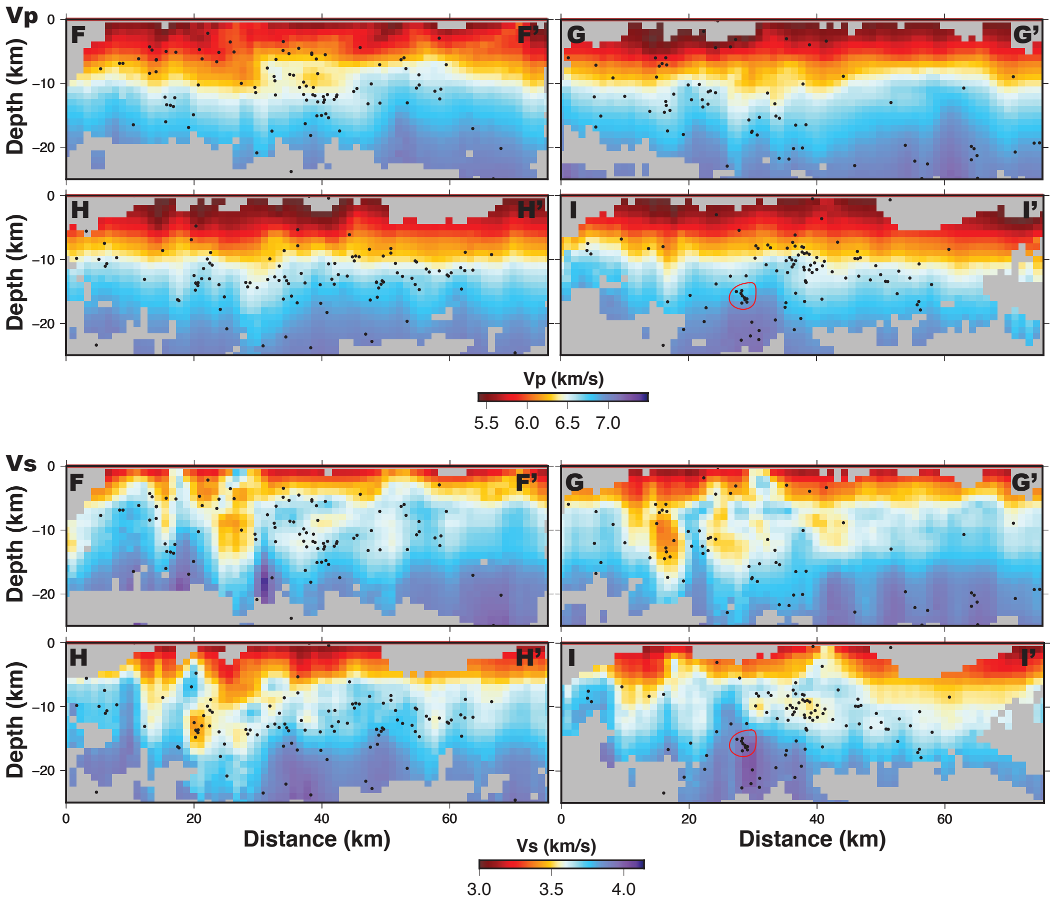

Figure 7. Vertical cross sections of profiles FF′-II′ for V_p (rows 1 & 2), and V_s (rows 3 & 4). Profiles lines are shown in Fig. 5. Red circle highlights an earthquake cluster in the middle crust within the impact structure near the south shore of St. Lawrence River.

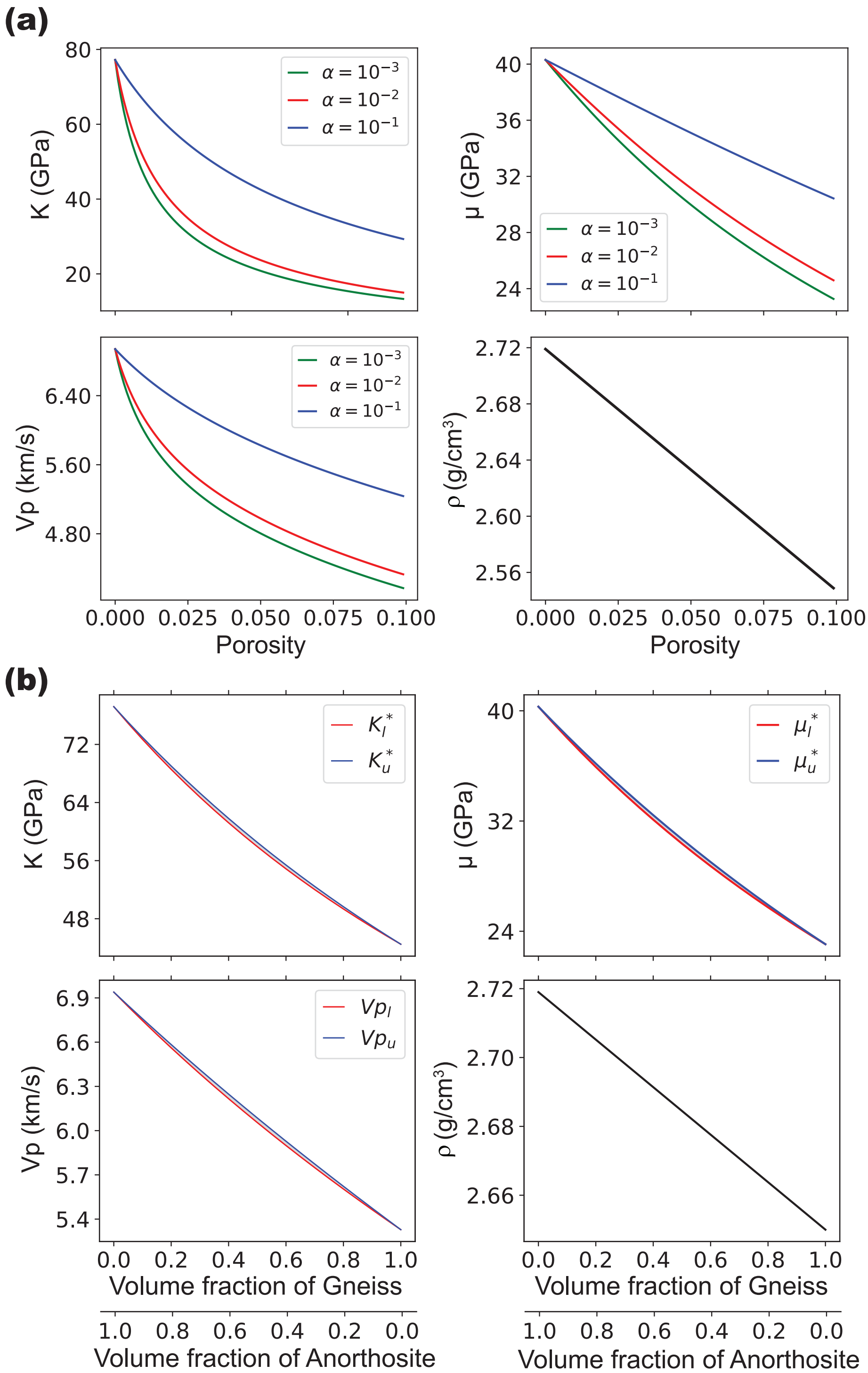

Figure 8. (a) Effective media analysis for a two-phase (anorthosite and water) media using the Kuster and Toksöz (1974) theoretical formulation. K, μ, ρ, and α represent bulk modulus, shear modulus and density of the effective medium, and crack aspect ratio. (b) Effective media analysis of a two-phase (anorthosite and gneiss) media derived with the theoretical relationship of Hashin and Shtrikman (1963). K_l^*, K_u^*, μ_l^*, μ_u^*, Vp_l, Vp_u represent the lower and upper bounds of bulk modulus, shear modulus and P-wave velocity of the effective medium. The proximity of the lower and upper bounds reflects the relative stiffness of the constitutive rocks.

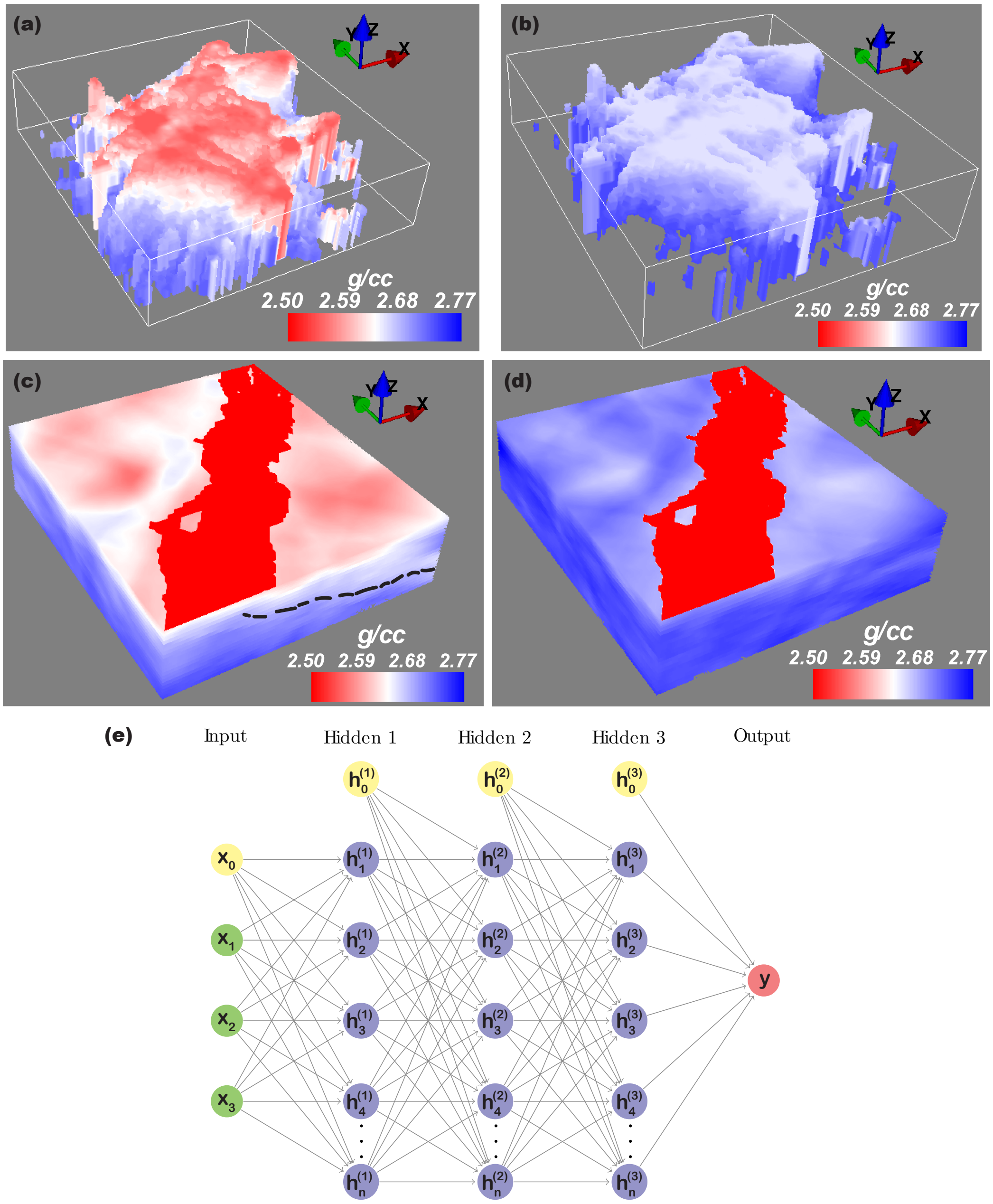

Figure 9. (a) & (b) Sparse 3D density model derived from effective media analysis with the Kuster and Toksöz (1974) and Hashin and Shtrikman (1963) theoretical formulations respectively. The sparse 3D density models are used as input for the neural network Multi-Layer Perceptron regression. (c) & (d) Full 3D density models determined from the regression analysis of (a) & (b) respectively. (e) The neural network with 3 hidden layers of 100 neurons each used for the Multi-Layer Perceptron regression. Dashed-black line in (c) could be the contact between Grenville Province and Appalachian rocks.

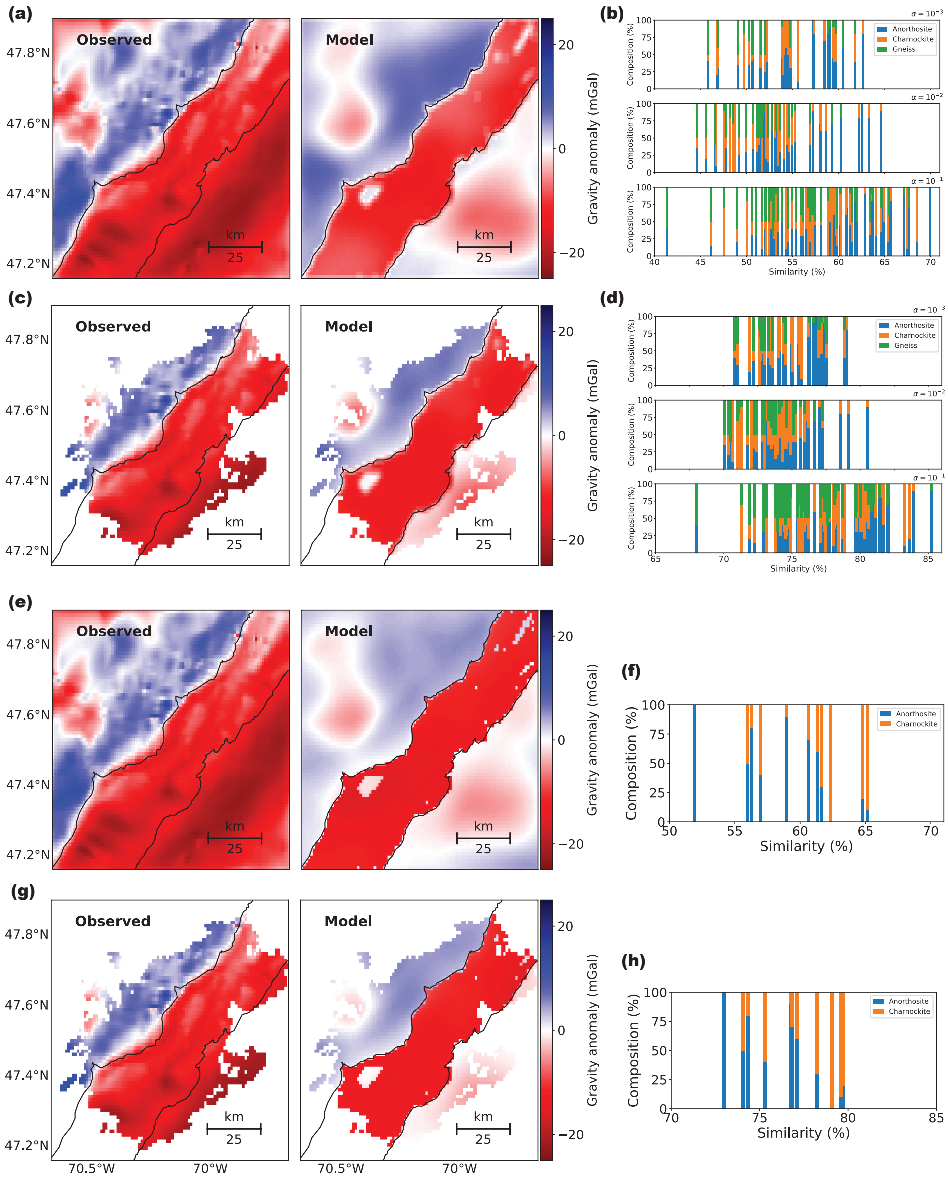

Figure 10. (a) & (b) Observed and best predicted residual gravity anomalies for the entire study area and respective similarity values for the intense fracturing scenario. (c) & (d) Observed and predicted residual gravity anomalies for the area with dense ray coverage (Fig. 2), and respective similarity values for the intense fracturing scenario. (b) & (d) show similarity of residual gravity anomaly predicted with the 165 3D density models to the observed Bouguer residual anomaly. (e) & (f) Observed and best predicted residual gravity anomalies for the entire study area, and respective similarity values for the compositional variation scenario. (g) & (h) Observed and best predicted residual gravity anomaly for the area with dense ray coverage, and respective similarity values for the compositional variation scenario. The predicted residual gravity anomaly was calculated with the same density model as in (e). (f) & (g) show similarity of residual gravity anomaly predicted with the 11 3D density models to the observed Bouguer anomaly.

Supporting Information for "Crustal velocity variations and constraints on material properties in the Charlevoix Seismic Zone, eastern Canada"

J. Onwuemeka[1]*, Y. Liu[1], and R. M. Harrington[2]

[1]Department of Earth and Planetary Sciences, McGill University, Montreal, Quebec, Canada

[2]Institute of Geology, Mineralogy and Geophysics, Ruhr University, Bochum, Germany

Contents of this file

S1 Traveltime tomography and hypocenter relocation We jointly invert for hypocenter and velocity structure in the Charlevoix seismic zone using body wave phase traveltime information of 2405 earthquakes reported between January, 1988, and May, 2019. We perform robust synthetic (checkerboard) tests to quantify the capability of the inversion algorithm and ability of the data set to resolve velocity structure. Steps in the synthetic test include tests for influences of grid size parameterization, checkerboard size, source-station geometry, forward solver, and starting velocity models. The synthetic travel times were generated with the catalog source-station geometries and the forward solver implemented in *TomoDD*. The inversion was performed with *LOTOS* to eliminate potential biases and errors in the forward solver. The results show that the main features in the checkerboard were recovered irrespective of the grid size parameterization, source-station geometry, and starting velocity model. The checkerboard recovery inverted with velocity model shown in Figure S1b is the most impacted. The checkerboard recovery diminishes with decreasing checkerboard size due to decreasing ray density within the checkerboard cubes.

Following results of the synthetic test, we performed tomographic inversion with the real data with grid size parameterization of 1 km and the south shore velocity model of (Lamontagne, 1999), as they both yield the lowest RMS error for V_p and V_s. The relocated hypocenters are shown in Fig. S12. The map and cross-sectional views of the V_p/V_s models are

*Current address: Dept. of Earth and Planetary Sciences, McGill University, Montreal, Quebec, Canada

shown in Figs. S14 & S14. The cross-sectional profiles were chosen to highlight velocity variations with the highly damaged crust due to the meteorite impact and the surroundings. For example, profile EE' shows velocity variations outside the impact zone, whereas the NE-SW profiles are intended to show variations within and outside the impact structure on single profiles.

S2 Gravity predictions We calculate the synthetic residual Bouguer anomaly with the complete 3D density models determined from intense fracturing and compositional variation scenarios. The 3D density models are divided into 3D voxels of the same grid spacing as the tomographic model. Each voxel in the 3D models is approximated by a sphere and the gravitational anomaly of each spherical mass point is calculated with in the wavenumber domain using the following expression, respectively (Li, 2010; Schmidt et al., 2010, 2011):

$$\mathcal{F}[g(\mathbf{K})] = 2\pi G \mathcal{F}[\Delta\rho(\mathbf{K})] \tag{1}$$

where G, $\Delta\rho$, R, and x, y, z, F, and $\mathbf{K}$ are the gravitational constant, density contrast, radius of sphere, and components of distance between mass point location and observation point (i.e. gravity station), Fourier transform, and wavenumber vector, respectively. In the wavenumber domain, each voxel is divided into a number of horizontal laminas that represent density sheets. The gravitational attraction of each laminae is calculated with a Fast Fourier Transform (FFT), filtered, and transferred to spatial domain with the inverse FFT. The vertical gravitational component of all the laminas in a voxel is summed to derived the vertical gravity component of the voxel.

The observed gravity anomalies were rediscretized to match the grid size and spacing of the model (Fig. S15). The best 5 predicted gravity anomalies that more closely match observed residual Bourguer anomaly for both scenarios is shown in Figures S18 - S21.

S3 Data and model limitations The traveltime data set contains a mix of manual and automatic arrival time picks. The traveltime data are retrieved from the Geological survey of Canada (GSC) and (Yu et al., 2016), whereas the rest of the arrival time data were manually picked by the authors. Due to data sparsity within the upper 2 km, tomography result for depths less than 2 km are less well-constrained. The neural network does not return a 100% cross-validation score for any of the model, hence some of the predicted densities may be slightly different from the input (Fig. S17). The cross-validation scores were not less than 80% and the neural network predicted most of the major gravity anomalies in the observation (Figs. S18 & S20), hence, density prediction error are within tolerable limits.

References

Lamontagne, M. (1999). Rheological and geological constraints on the earthquake distribution in the charlevoix seismic zone, quebec, canada. *Ph.D. thesis, Carleton University, (Geological Survey of Canada Open File Report D-3778).*

Li, X. (2010). Efficient 3d gravity and magnetic modeling. In *Proceedings of egm 2010 international workshop.*

Schmidt, S., Götze, H.-J., Fichler, C., & Alvers, M. (2010). Igmas+–a new 3d gravity, ftg and magnetic modeling software. *GEO-INFORMATIK Die Welt im Netz, edited by: Zipf, A., Behncke, K., Hillen, F., and Scheffermeyer, J., Akademische Verlagsgesellschaft AKA GmbH, Heidelberg, Germany*, 57–63.

Schmidt, S., Plonka, C., Götze, H.-J., & Lahmeyer, B. (2011). Hybrid modelling of gravity, gravity gradients and magnetic fields. *Geophysical Prospecting*, *59*(Advances in Electromagnetic, Gravity and Magnetic Methods for Exploration), 1046–1051.

Yu, H., Liu, Y., Harrington, R. M., & Lamontagne, M. (2016). Seismicity along st. lawrence paleorift faults overprinted by a meteorite impact structure in charlevoix, québec, eastern canada. *Bulletin of the Seismological Society of America*, *106*(6), 2663–2673.

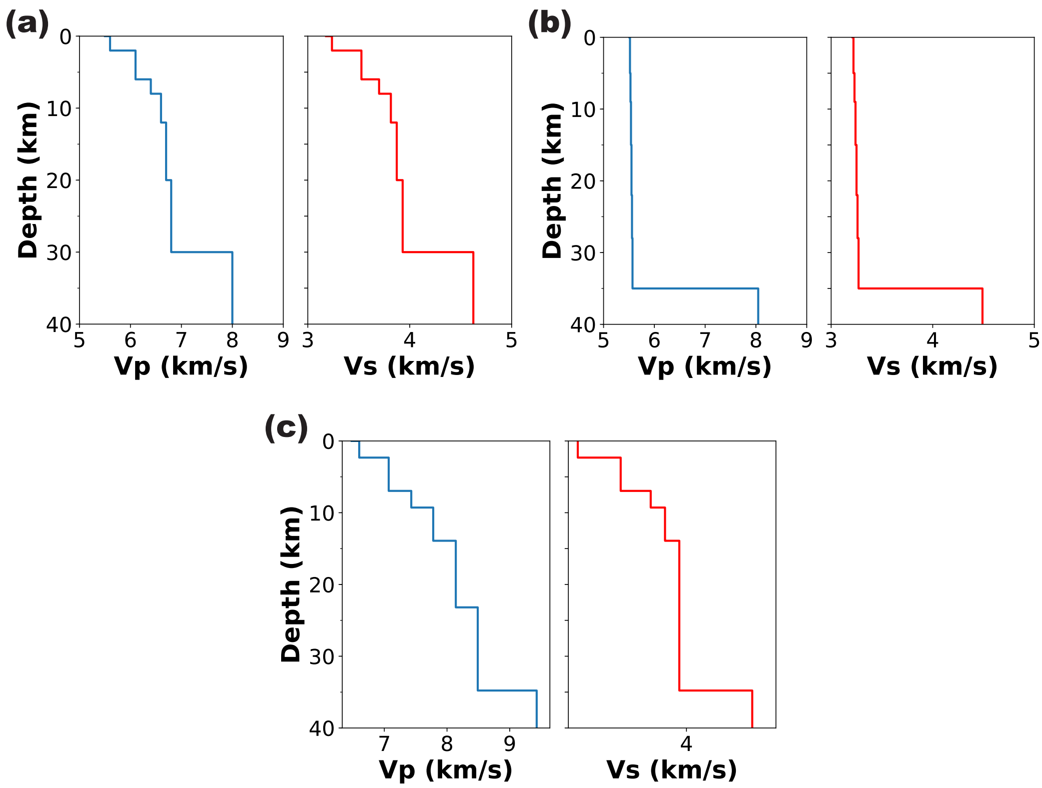

Figure S1. (a) The south shore velocity model of Lamontagne (1999). (b) a quasi layer-over-halfspace velocity model. (c) A perturbed velocity model determined by randomised perturbation of (a).

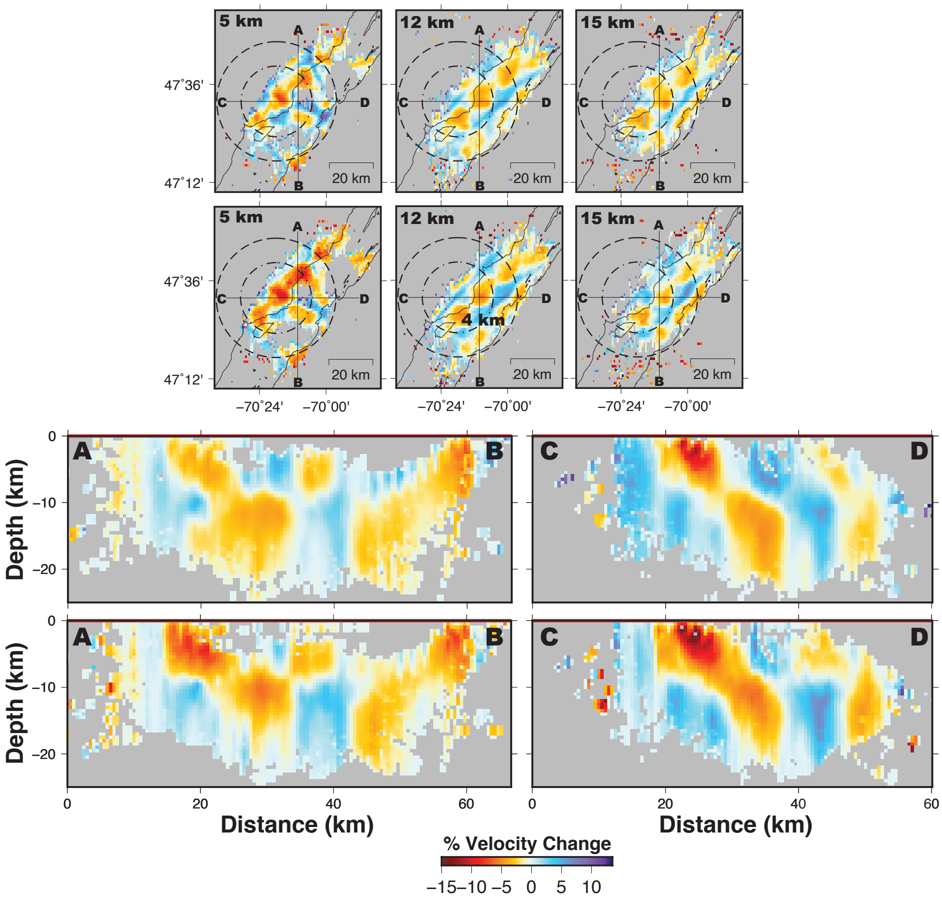

Figure S2. Checkerboard recovery with grid size parameterization of 0.5 km.

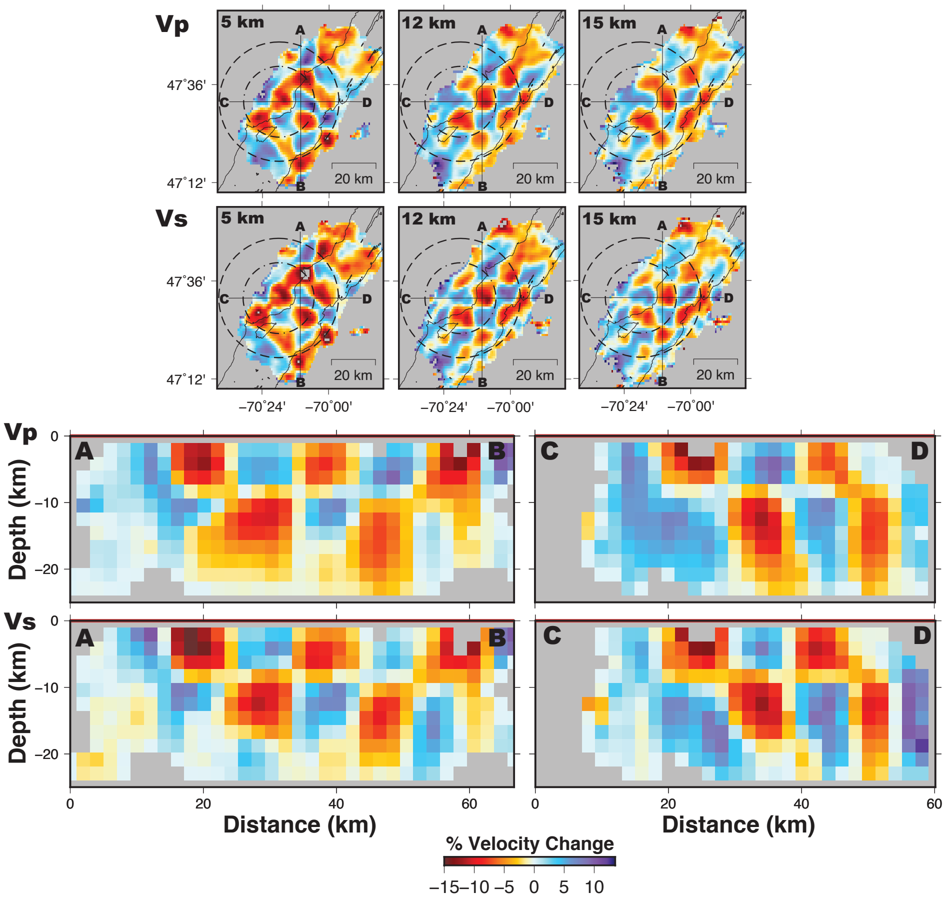

Figure S3. Checkerboard recovery with grid size parameterization of 2 km.

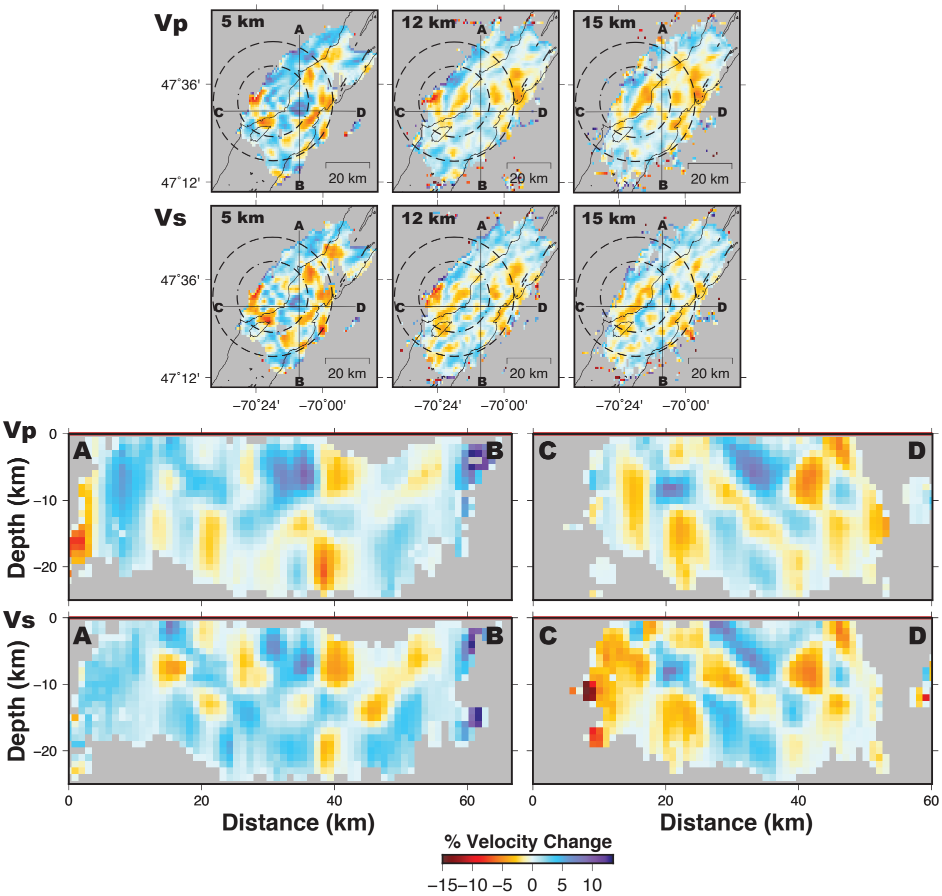

Figure S4. Checkerboard recovery for 6 km checkerboard size and grid size parameterization of 1 km.

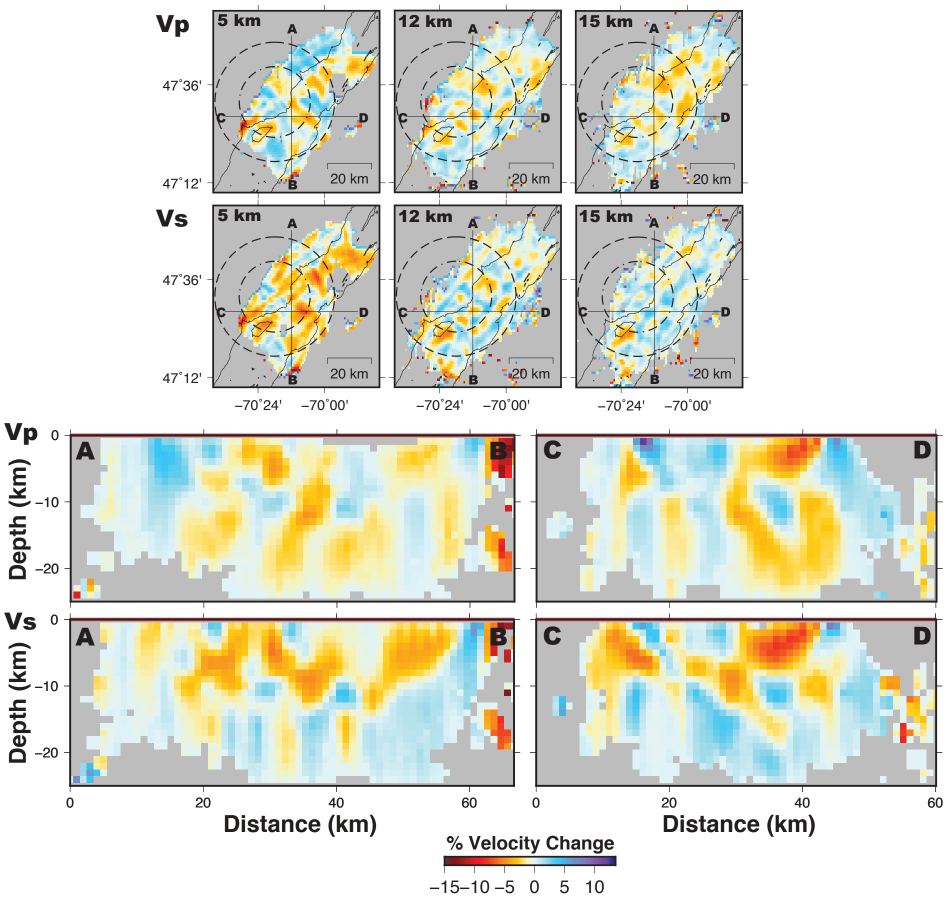

Figure S5. Checkerboard recovery for 5 km checkerboard size and grid size parameterization of 1 km.

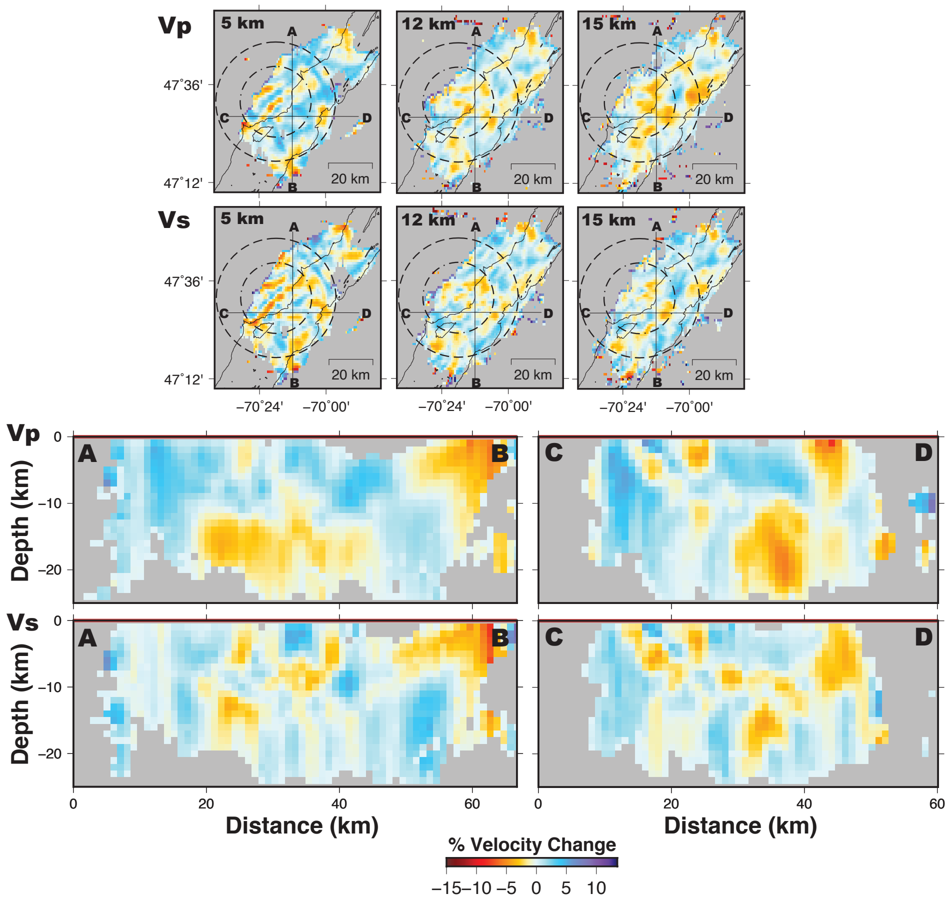

Figure S6. Checkerboard recovery for 4 km checkerboard size and grid size parameterization of 1 km.

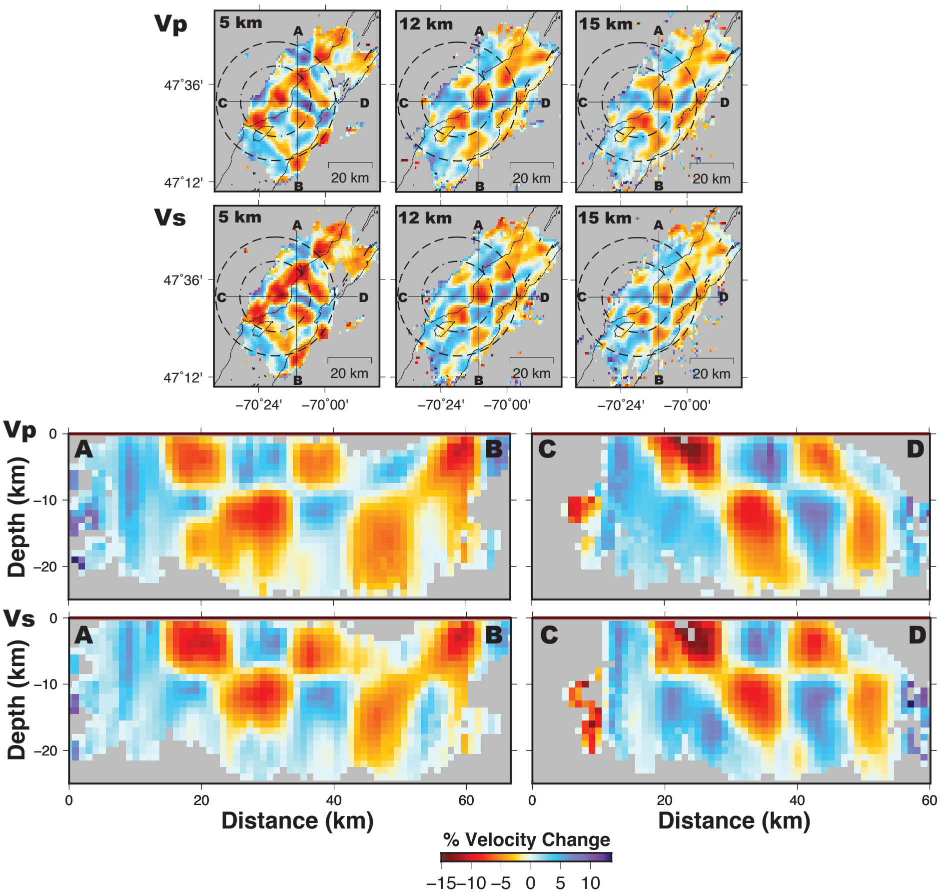

Figure S7. Checkerboard recovery for 10 km checkerboard size and grid size parameterization of 1 km. All the events are placed at 1 km depth in the middle of the study area.

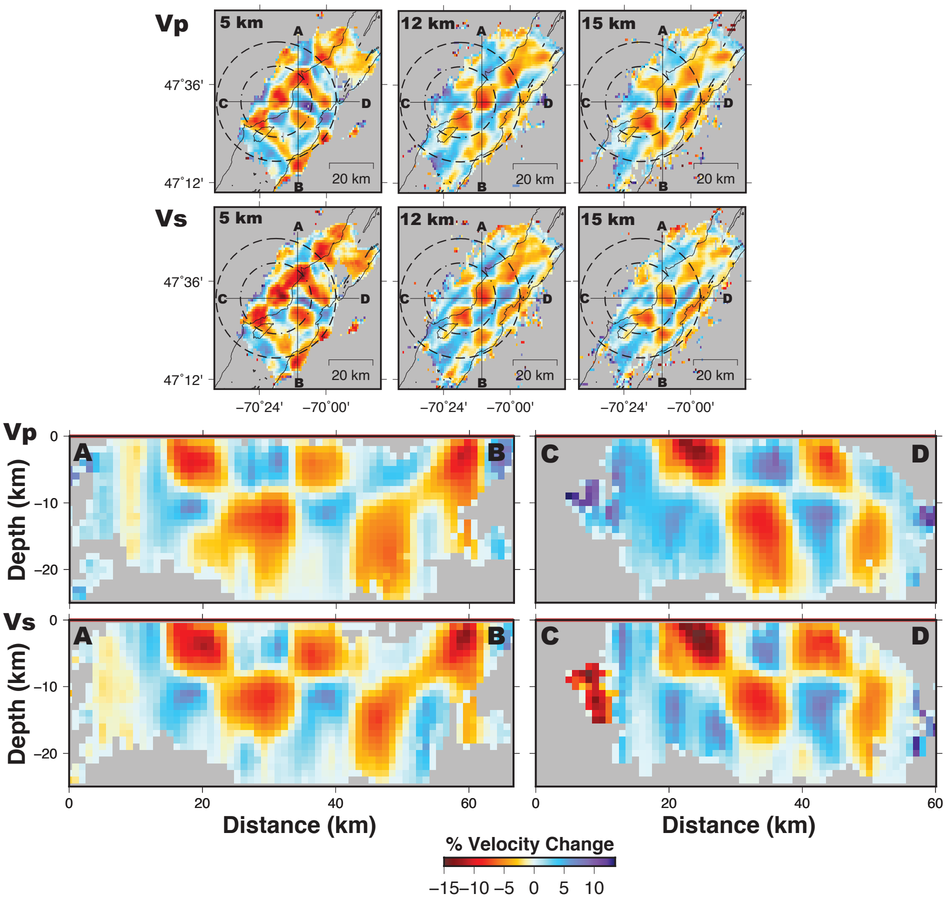

Figure S8. Checkerboard recovery for 10 km checkerboard size and grid size parameterization of 1 km. All events are initially placed at 5 km depth in the middle of the study area.

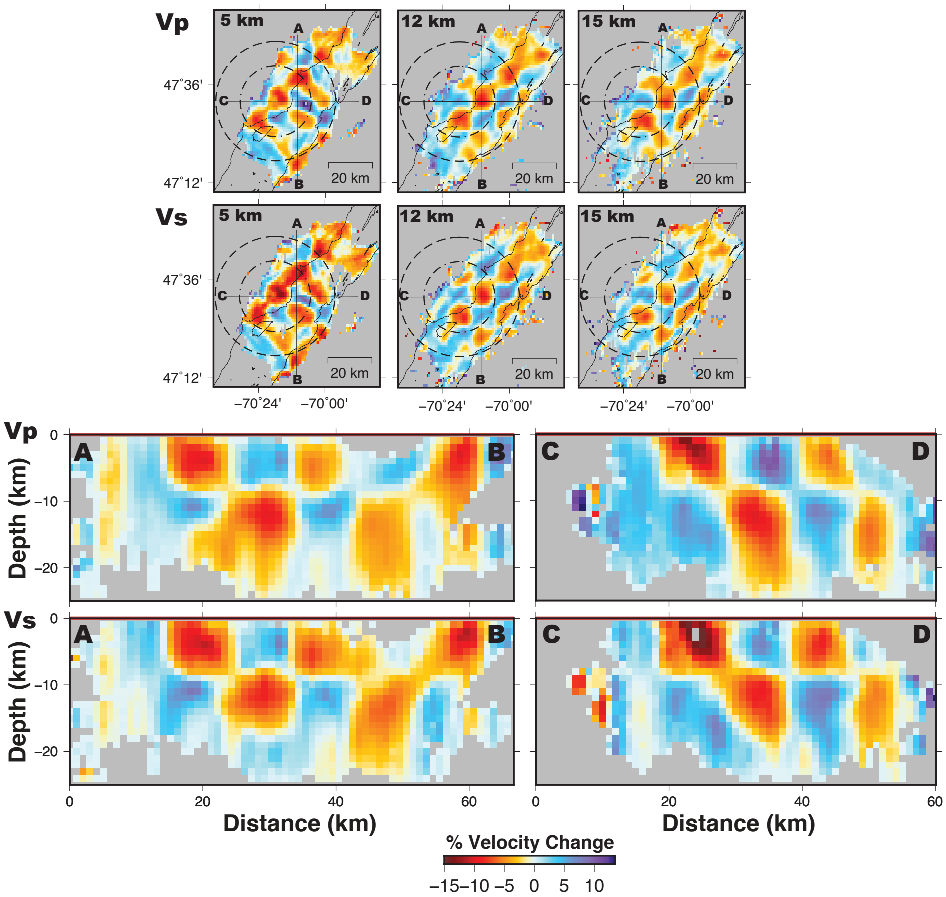

Figure S9. Checkerboard recovery for 10 km checkerboard size and grid size parameterization of 1 km. All events are initially placed at 10 km depth in the middle of the study area.

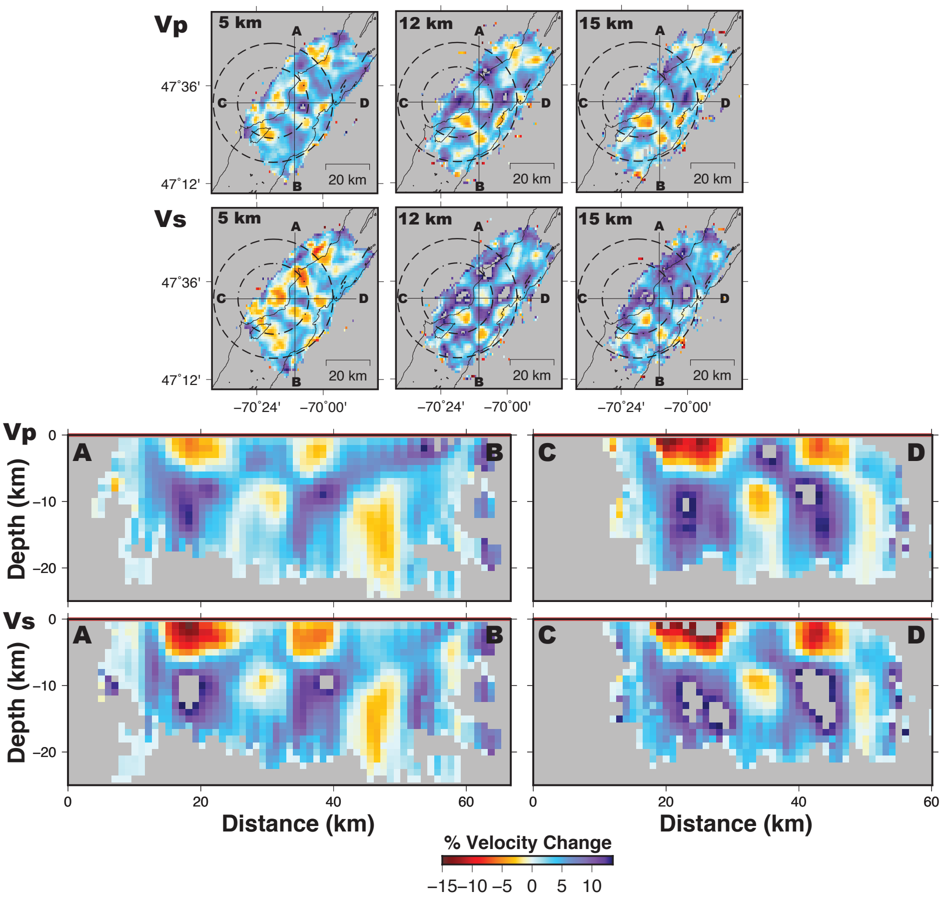

Figure S10. Checkerboard recovery for 10 km checkerboard size, grid size parameterization of 1 km, and starting velocity model Fig. S1b.

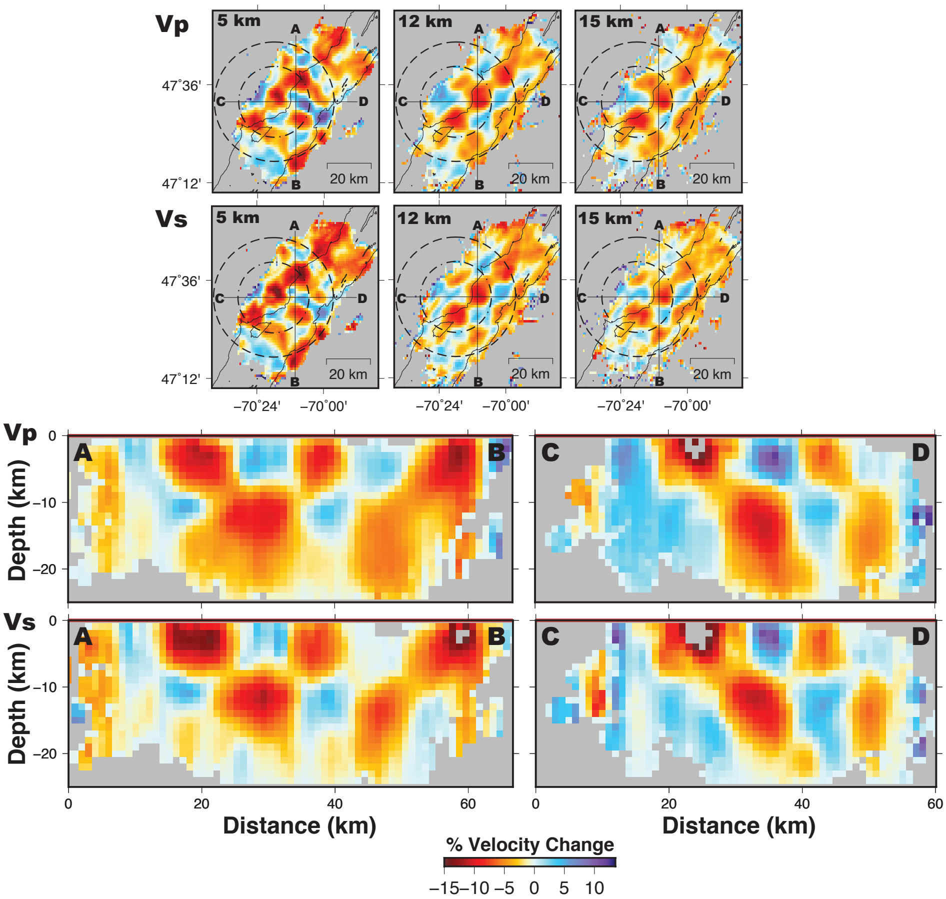

Figure S11. Checkerboard recovery for 10 km checkerboard size, grid size parameterization of 1 km, and starting velocity model Fig. S1c.

Figure S12. Relocated hypocenters of 1557 earthquakes in the study area.

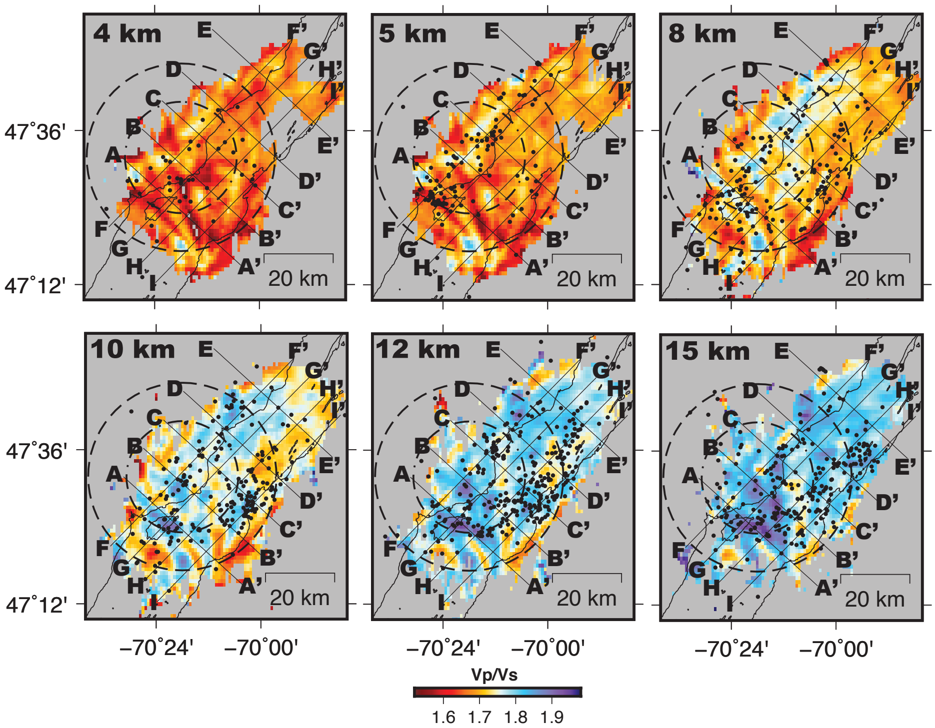

Figure S13. Map view of V_p/V_s variation.

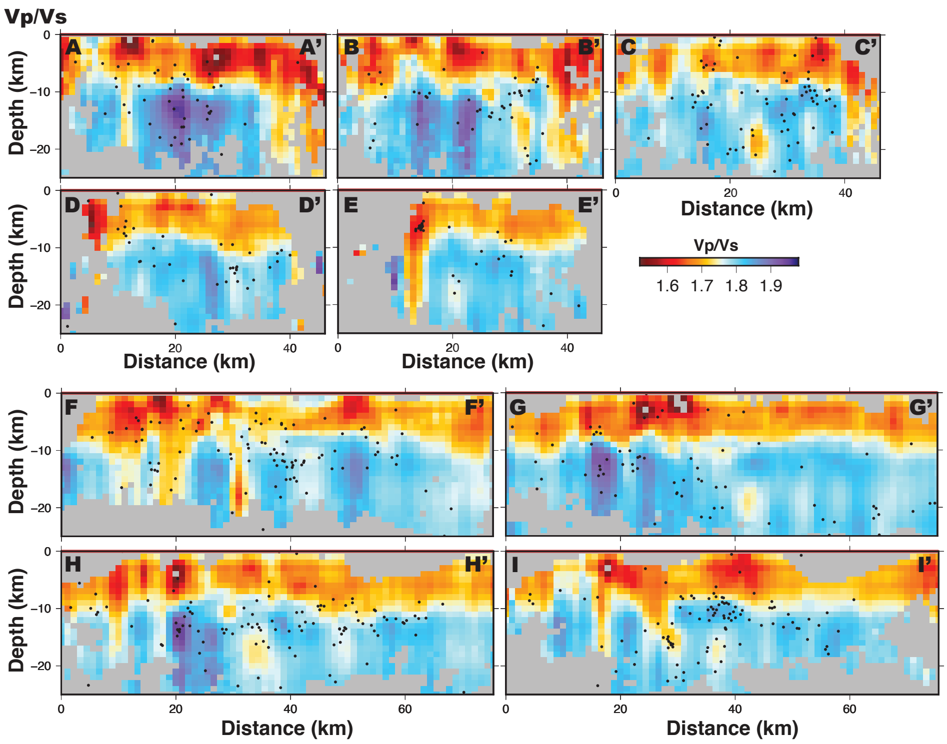

Figure S14. Cross-sectional view of V_p/V_s variation.

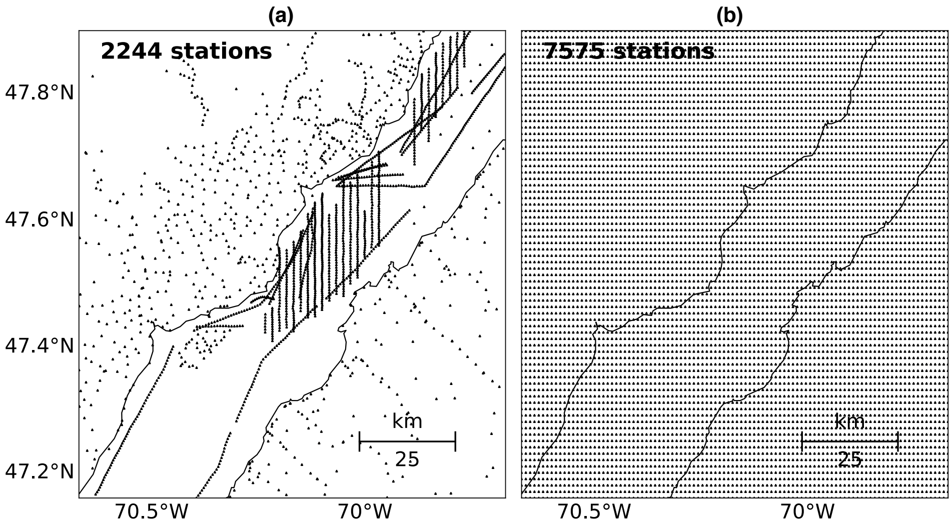

Figure S15. (a) Original Bouguer anomaly data points. (b) Interpolated Bouguer anomaly data points.

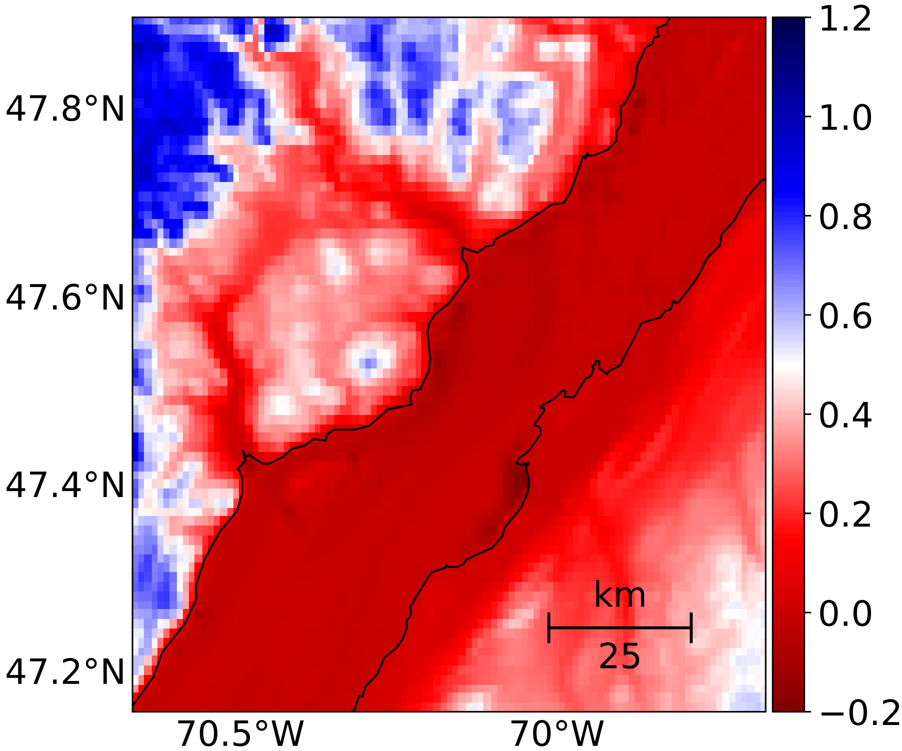

Figure S16. Topography map of the study area.

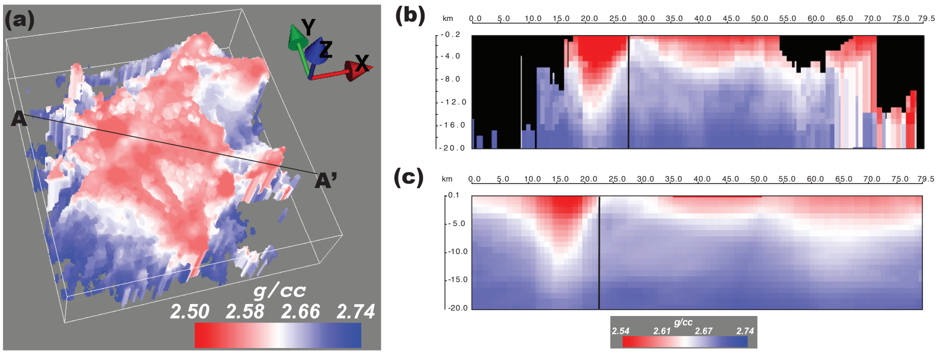

Figure S17. (a) Same as in Fig. 9a. (b) Cross-sectional view of densities along profile AA' before MPL regression. (c) Cross-sectional view of densities along profile AA' after MPL regression. The vertical black lines in (b) & (c) highlight a $\sim$ 5 km shift of the low-density body to the left of the lines.

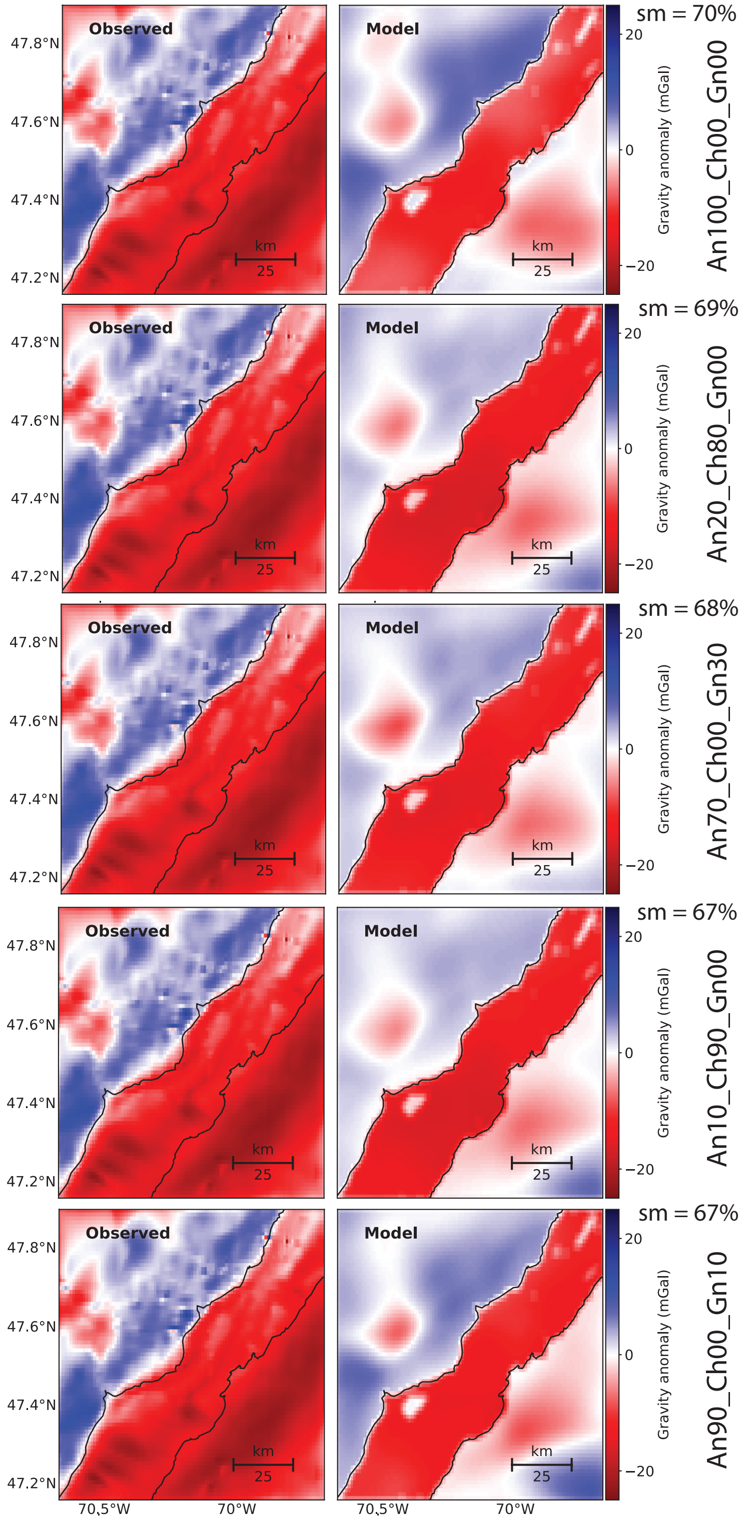

Figure S18. The five best predicted gravity anomalies of the entire study area for the intense fracturing scenario. The percent composition of the 3 rock types and similarity measure (sm) of the fits are indicated.

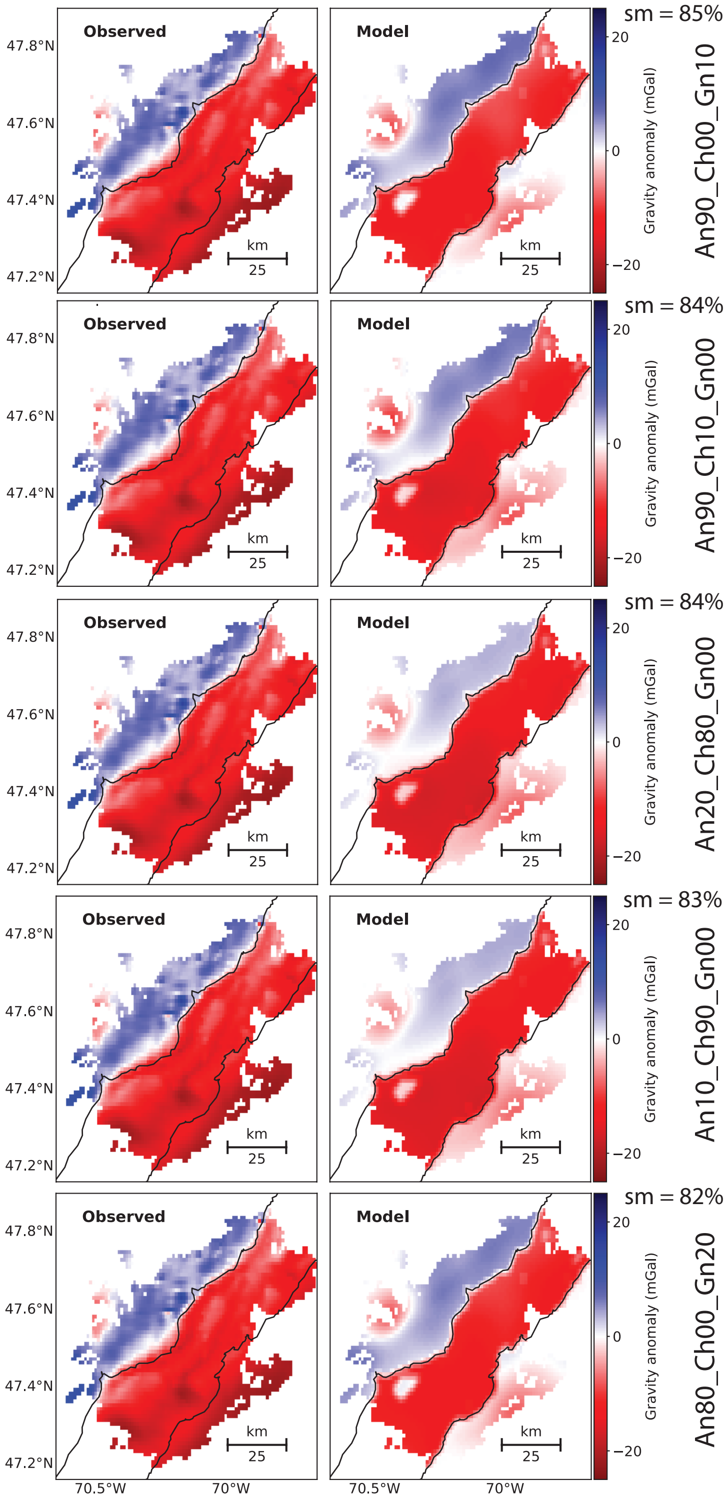

Figure S19. The five best predicted gravity anomalies of the section of the study area with dense ray coverage for the intense fracturing scenario. The percent composition of the 3 rock types and similarity measure (sm) of the fits are indicated.

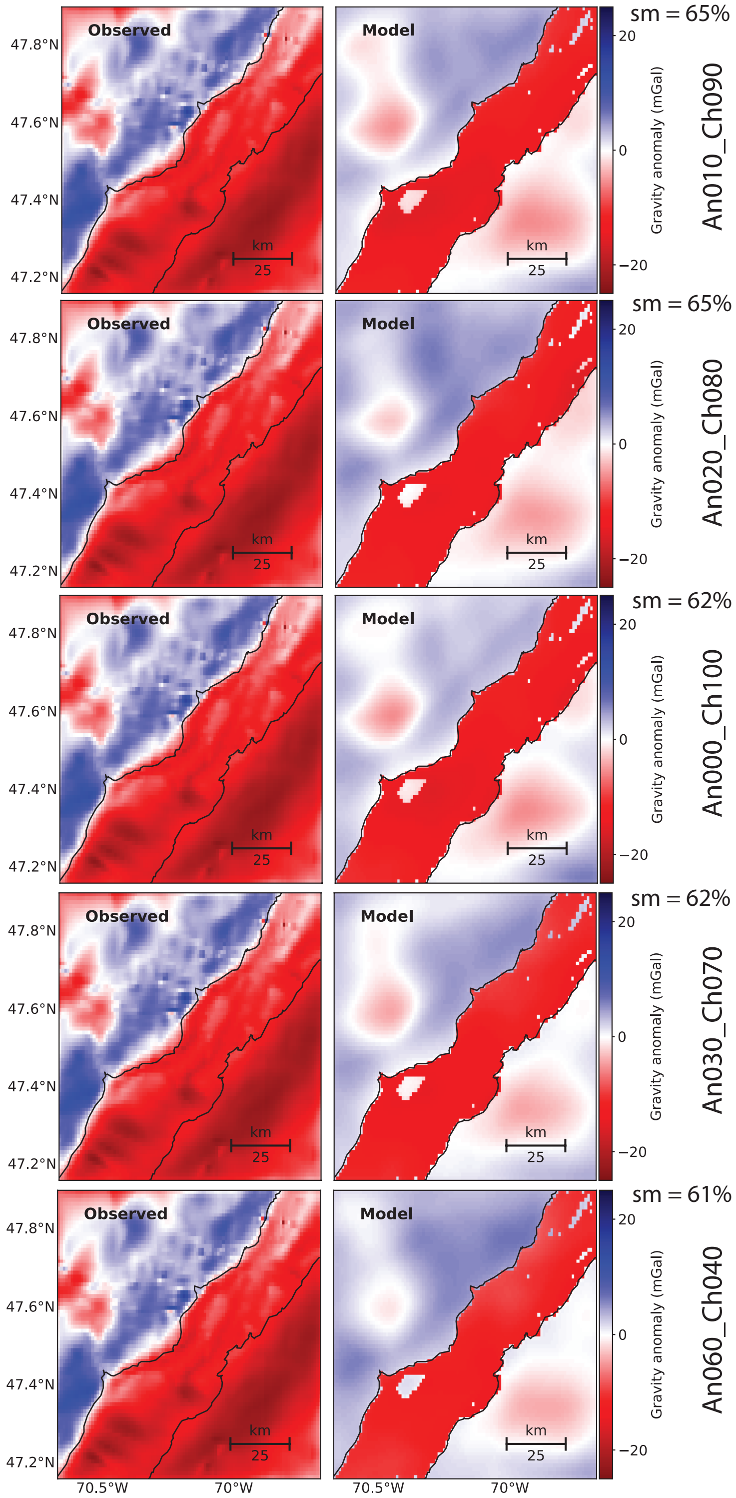

Figure S20. The five best predicted gravity anomalies of the entire study area for the compositional variation scenario. The percent composition of anorthosite and charnockite in the composite rock (i.e. phase 1) and similarity measure (sm) of the fits are indicated.

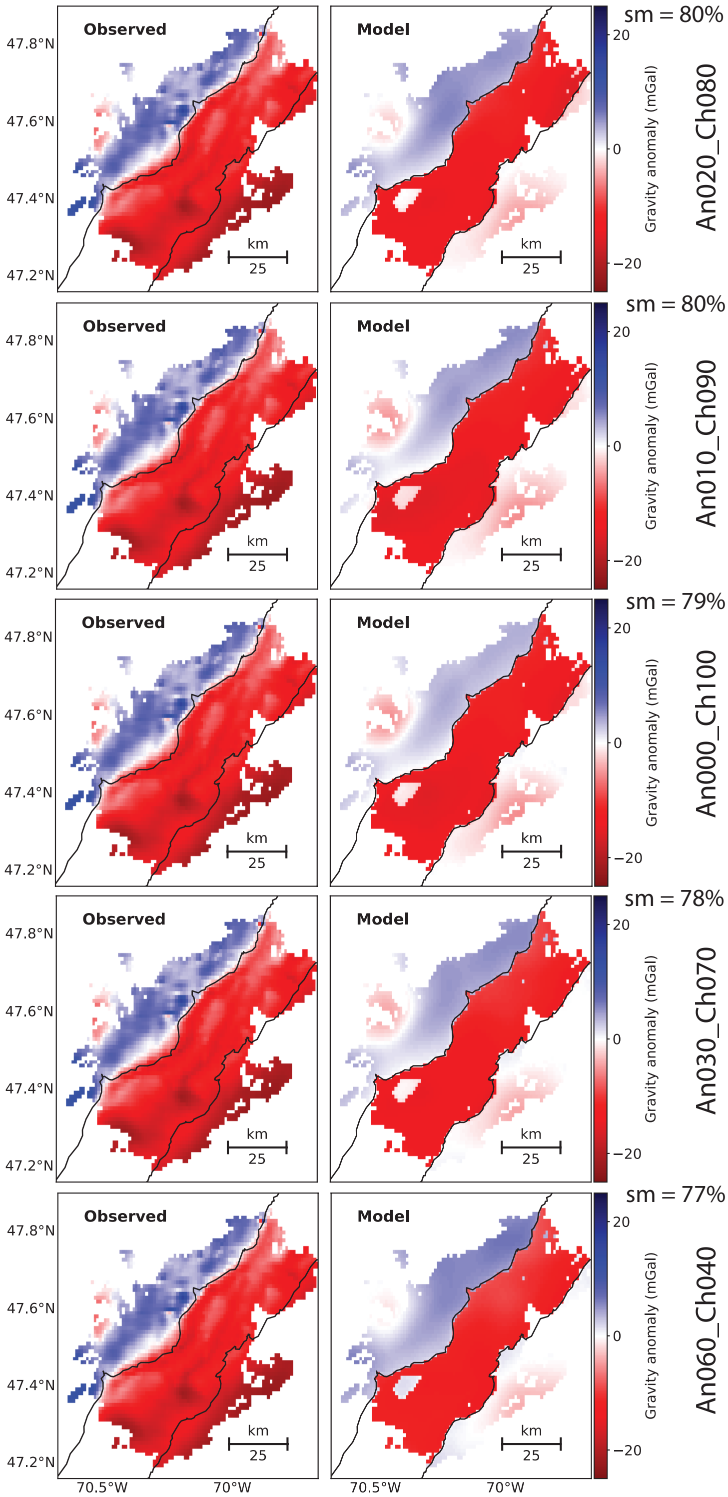

Figure S21. The five best predicted gravity anomalies of the section of the study area with dense ray coverage for the compostional variation scenario. The percent composition of anorthosite and charnockite in the composite rock (i.e. phase 1) and similarity measure (sm) of the fits are indicated.